JGR Solid Earth

RESEARCH ARTICLE
10.1029/2024JB029063

Numerical Simulation on the Electrical Conductivity of Ternary Mixtures Containing NaCl Solution, Quartz, and Smectite

K. Aoyama[1] **and T. Hashimoto**[2]

[1]Graduate School of Science, Hokkaido University, Sapporo, Japan, [2]Faculty of Science, Hokkaido University, Sapporo, Japan

Key Points:

- A simulator was developed to compute the bulk electrical conductivity of rocks containing an aqueous NaCl solution, quartz, and smectite
- The simulator reproduced the experimental conductivity measurements by giving the anisotropy of the components' distribution
- The bulk conductivity of smectite-rich rocks exhibited a partial decrease with an increasing salinity or macroporosity

Correspondence to:
K. Aoyama,
aoyama.kentaro.k0@elms.hokudai.ac.jp

Citation:
Aoyama, K., & Hashimoto, T. (2024). Numerical simulation on the electrical Conductivity of ternary mixtures containing NaCl solution, quartz, and smectite. *Journal of Geophysical Research: Solid Earth*, *129*, e2024JB029063. https://doi.org/10.1029/2024JB029063

Received 8 MAR 2024
Accepted 8 OCT 2024

Author Contributions:
Conceptualization: K. Aoyama, T. Hashimoto
Data curation: K. Aoyama
Formal analysis: K. Aoyama
Methodology: K. Aoyama
Software: K. Aoyama
Supervision: T. Hashimoto
Validation: K. Aoyama
Visualization: K. Aoyama
Writing – original draft: K. Aoyama
Writing – review & editing: T. Hashimoto

Abstract While the electrical conductivity of smectite-rich rocks is high, previous studies have only partially revealed its dependence on temperature, salinity, and porosity. This knowledge gap mainly arises from challenges in controlling various experimental conditions when measuring the conductivity of real smectite-bearing rock samples and quantifying the smectite content. To mimic conductivity measurements under ideal conditions, this study aimed to develop a simulator capable of accurately configuring the conditions to predict the direct-current conductivity of saturated rocks composed of an aqueous NaCl solution, quartz, and smectite under various temperatures (20°C–200°C), salinities (10^{-4}–5 mol kg^{-1}), porosities (0–1), and smectite fractions (0–1). The simulator reproduced the experimental conductivity measurements from drilled core samples by giving the anisotropy of those components' distribution. In addition, simulations with randomly assigned components revealed that when rocks contain abundant smectite, the bulk conductivity partially decreases with increasing NaCl solution's salinity or volume fraction. These negative slopes were approximated using empirical equations derived from previous studies. Percolation analysis further revealed that when the components are randomly assigned, conductive paths begin to form between the ends of the modeled sample once the sum of the volume fraction of bulk pore and smectite reaches 0.1.

Plain Language Summary When a rock contains smectite—a clay mineral commonly found in shallow parts of the ground—its electrical conductivity is known to increase. However, the detailed relationships between the conductivity of such smectite-bearing rocks and temperature, salt concentration of pore water, and the amount of fluid and smectite remain to be clarified. Therefore, we developed a simulator applicable to various physical and chemical conditions and attempted to clarify these relationships through numerical simulation. First, we confirmed that our simulator can reproduce the reported experimental results using real rock samples. While it is established that rock conductivity increases with higher fluid volume fractions and salinity, our simulations revealed a counterintuitive phenomenon: when smectite is abundant, rock conductivity partially decreases with increasing salinity or fluid content within large pores. We approximated this behavior using an empirical equation proposed in a previous study by adding new parameters for salinity dependence. Furthermore, our simulations with randomly assigned components showed that when the volume fraction of large pores and smectite in the rock exceeds 10%, current pathways comprising these components begin to form, leading to a rapid increase in rock conductivity.

1. Introduction

Electromagnetic sounding is a prominent method for investigating subsurface structures because the electrical conductivity of rock serves as a good proxy for crucial geological and/or geophysical features, such as temperature, salinity of pore fluid, geometry of the pore network, and degree of clay alteration. Among them, smectite, a clay mineral commonly found in characteristic geological structures such as caprocks of a geothermal reservoir (e.g., Àrnason et al., 2000), landslide layers (e.g., Castro et al., 2020), and subducting plate boundaries (e.g., Vrolijk, 1990), is known to contribute to the increase in bulk conductivity of rocks (e.g., Lévy et al., 2018). However, the dependence of the conductivity of smectite-bearing rocks on temperature, fluid salinity, porosity, and the amount of smectite has only been partially clarified by laboratory experiments in previous studies (e.g., Lévy et al., 2018; Waxman & Smits, 1968). The limited number of experimental studies is mostly due to the difficulty in accurately quantifying the smectite content and controlling the petrophysical properties of smectite-bearing rocks. For example, X-ray diffraction (XRD) is a common technique for quantifying clay minerals;

however, because of the variable chemical compositions, structures, and preferred orientations of smectite, estimations of the clay mineral contents may contain significant uncertainties (Zhou et al., 2018). In addition, when measuring the conductivity of core samples containing smectite, great attention is required to avoid collapse or swelling of the samples at a low salt concentration (Takakura, 2009; Waxman & Smits, 1968), to leave them for months for equilibrium at a high concentration (Waxman & Smits, 1968), and to maintain a constant temperature (Kaufhold et al., 2014). Although numerical simulations have the advantage of controlling those petrophysical conditions and mimicking experimental measurements (e.g., Fu et al., 2021), to the authors' knowledge, no simulator universally applies to a wide range of temperatures, pressures, and salinities for rocks containing clay minerals.

Therefore, this study aimed to develop a simulator that can accurately control the petrophysical conditions to predict the direct-current conductivity of saturated rocks composed of aqueous NaCl solution, quartz, and smectite under various temperatures (20°C–200°C), salinities (10^{-4}–5 mol kg^{-1}), porosities (0–1), and smectite fractions (0–1). Simulations were performed in the following steps, as outlined comprehensively in Section 2: (1) calculating the conductivity of each component constituting the rock (Section 2.1), (2) assigning each component in a discretized space (Section 2.2), and (3) computing the current density from the electric potential distribution using the finite element method (FEM) (Section 2.3). The simulation results were compared with experimental data and empirical equations from previous studies. Furthermore, this study investigated the effect of the smectite content on the percolation threshold.

2. Method

2.1. Conductivity of Each Component

As a first step, we calculated the conductivities of NaCl solution, quartz, and smectite across varied temperatures (20°C–200°C), pressures (0.1–5 MPa), and salt concentrations (10^{-4}–5 mol kg^{-1}). In addition, we calculated the conductivities of the electrical double layers (EDLs) formed at solid–liquid boundaries (i.e., the boundaries between quartz and aqueous NaCl solution and between smectite and aqueous NaCl solution). These calculations were based on the model proposed in previous studies (Gonçalvès et al., 2007; Leroy et al., 2013, 2022; Leroy & Revil, 2004, 2009; Sen & Goode, 1992). In the following subsections, we first describe some physical and chemical properties of the NaCl solution necessary for the following steps and then explain the calculation of the electrochemical properties of the EDLs that develop on the surfaces of quartz and smectite.

2.1.1. Aqueous NaCl Solution

The electrical conductivity of the aqueous NaCl solution was calculated using an empirical equation proposed by Sen and Goode (1992) (Figure 1a):

$$\sigma_w = \left(5.6 + 0.27T_c - 1.5 \times 10^{-4}{T_c}^2\right)m - \frac{2.36 + 0.099T}{1 + 0.214m^{\frac{1}{2}}}m^{\frac{3}{2}}, \quad (1)$$

where σ_w is the conductivity of the NaCl solution (in S m^{-1}), T_c is the temperature (in °C), and m is the molality (in mol kg^{-1}). Watanabe et al. (2021) recommend the use of Sen and Goode's (1992) equation for low temperatures, as addressed in the present study (≤200°C) as it best reproduced the experimental data of Bannard (1975) measured under various pressures (25–200 MPa) and salinities (10^{-2}–5 M NaCl). The conductivity tensor of the NaCl solution is expressed in an isotropic form:

$$\boldsymbol{\sigma}_w = \begin{bmatrix} \sigma_w & 0 & 0 \\ 0 & \sigma_w & 0 \\ 0 & 0 & \sigma_w \end{bmatrix}. \quad (2)$$

This conductivity tensor will be assigned to each voxel in the discretized space of the numerical calculations.

We also calculated some physical and chemical properties of aqueous NaCl solution using models by Driesner (2007), Klyukin et al. (2017), Raspo and Neau (2020), and Pitzer (1973), which accurately reproduced

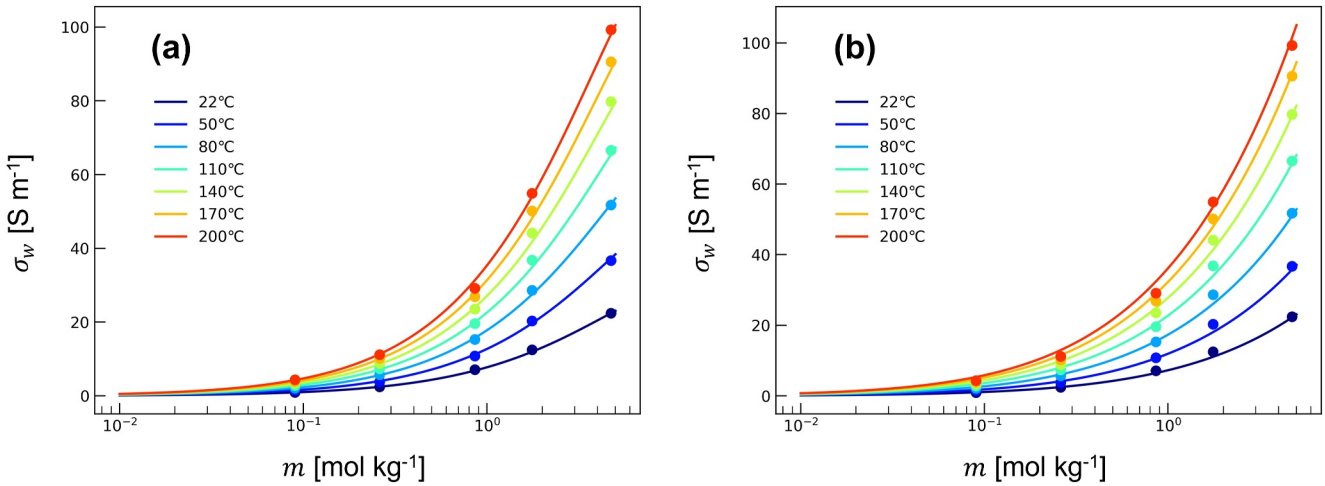

Figure 1. Electrical conductivity of aqueous NaCl solution as a function of molality. (a) Conductivity calculated using the empirical equation of Sen and Goode (1992). (b) Conductivity calculated from the ion mobility of Equation 3 (P = 5.0 MPa). In both figures, the dots represent the experimental data of Sen and Goode (1992), and the lines represent the calculated values.

experimental data across varied temperatures (20°C–200°C) and salinities (0–5 mol kg^{-1} NaCl) (Table 1). These properties will be used to calculate the electrochemical properties of the EDLs in Sections 2.1.2 and 2.1.3. It should be noted that the temperature dependences of Pitzer's parameters (Voigt, 2020) were fitted by the experimental data on the vapor–liquid–halite coexisting curve compiled by Cohen-Adad and Lorimer (1991). Therefore, the applicable pressure may be less than 1.1 MPa. However, the pressure dependence of the activity coefficient is expected to be sufficiently small (~10^{-8} Pa^{-1}) in the low-temperature (≤200°C) and low-pressure (≤5 MPa) conditions covered in the present study (e.g., Monnin, 1990). Therefore, we neglected the pressure dependence of Pitzer's parameters.

The mobilities of Na^+ and Cl^- in the pore water were calculated from the empirical equations devised in this study to align with the conductivity data of Sen and Goode (1992) (Figure 1b):

$$\beta_i^w = \beta_i^\circ(T, P)\left[\exp\left(-am^b\right) + \frac{c}{T}\right], \tag{3}$$

with

$$\beta_i^\circ(T, P) = \frac{eD_i^\circ \eta^\circ(298.15, P)}{298.15 k_B \eta^\circ(T, P)}, \tag{4}$$

where a, b, and c are free parameters optimized using the Levenberg–Marquardt method implemented in *lmfit* package (a software for nonlinear regression) (Newville et al., 2023) at 5 MPa (Table 2), $\beta_i^\circ(T,P)$ is the mobility

Table 1
List of Relevant Models for Calculating the Physical and Chemical Properties of Aqueous NaCl Solution

Properties	Symbols	Models	Temperature (°C)	Pressure (MPa)	Molality (mol kg^{-1})
Density (in kg m^{-3})	ρ_w	Driesner (2007) [a]	0–1000	0.1–500	0–m_{sat}
Dynamic viscosity (in Pa s)	η_w	Klyukin et al. (2017)	0–1000	0.1–500	0–m_{sat}
Dielectric permittivity (in F m^{-1})	ε_w	Raspo and Neau (2020)	30–325	3×10^{-3}–11.8 [b]	0–10.41
Ion activity	a_i^w	Pitzer (1973) [c]	0–200	Not provided	0–m_{sat}

Note. The temperature, pressure, and molality columns indicate the models' applicability ranges. m_{sat} denotes the molality of the halite-saturated liquid. [a]We used the parameters optimized for IAPWS-95, as suggested by Mao et al. (2015). [b]Experimental data cover this range, but empirical parameters used to compute dielectric permittivity do not consider the pressure dependences. [c]Pitzer's equation was calculated by considering the temperature dependence of the Pitzer's parameters suggested by Voigt (2020).

Table 2
Parameter Values for Calculating the Mobility of Ions in Pore Water (Equations 3 and 4)

Symbols	Values
a (mol^{-1} kg)	1.1845
b	0.38359
c (K)	94.931
$D^{\circ}_{Na^+}$ (m^2 s^{-1})	1.33×10^{-9}
$D^{\circ}_{Cl^-}$ (m^2 s^{-1})	2.03×10^{-9}

(m^2 s^{-1} V^{-1}) of ion i at infinite dilution in water at temperature T (in K) and pressure P (in Pa), e is the elementary charge (1.602×10^{-19} C), D°_i is the self-diffusion coefficient (m^2 s^{-1}) of ion i at infinite dilution in water at 25°C derived from Roger et al. (2009) (Table 2), and $\eta^{\circ}(T, P)$ is the dynamic viscosity (Pa s) of pure water calculated by the formulation of the International Association for the Properties of Water and Steam 2008 (IAPWS, 2008) implemented in *the iapws* package (Romera, 2021).

2.1.2. Quartz

In the temperature range for smectite-rich formations (≤~200°C), the atomic bonds in quartz are ionic or covalent, and the atoms strongly bind the electrons. The electrical conductivity is around 10^{-12} S m^{-1} (Watanabe, 2005; Yamamoto & Namikawa, 1994). While the conductivity of quartz is temperature dependent, its slope in the above temperature range is less than 10^{-11} S m^{-1} K^{-1} (Yamamoto & Namikawa, 1994), which is negligible compared to the effects of NaCl solution and EDL. Therefore, the conductivity of quartz was assumed to be constant and set to 10^{-12} S m^{-1}. The constant conductivity tensor of quartz can be expressed in isotropic form:

$$\boldsymbol{\sigma}_{quartz} = \begin{bmatrix} 10^{-12} & 0 & 0 \\ 0 & 10^{-12} & 0 \\ 0 & 0 & 10^{-12} \end{bmatrix}. \quad (5)$$

The electrochemical properties of the EDL that develops between quartz and pore water were calculated using the 1-pK basic Stern model (BSM) developed by Leroy et al. (2013, 2022) (Figure 2):

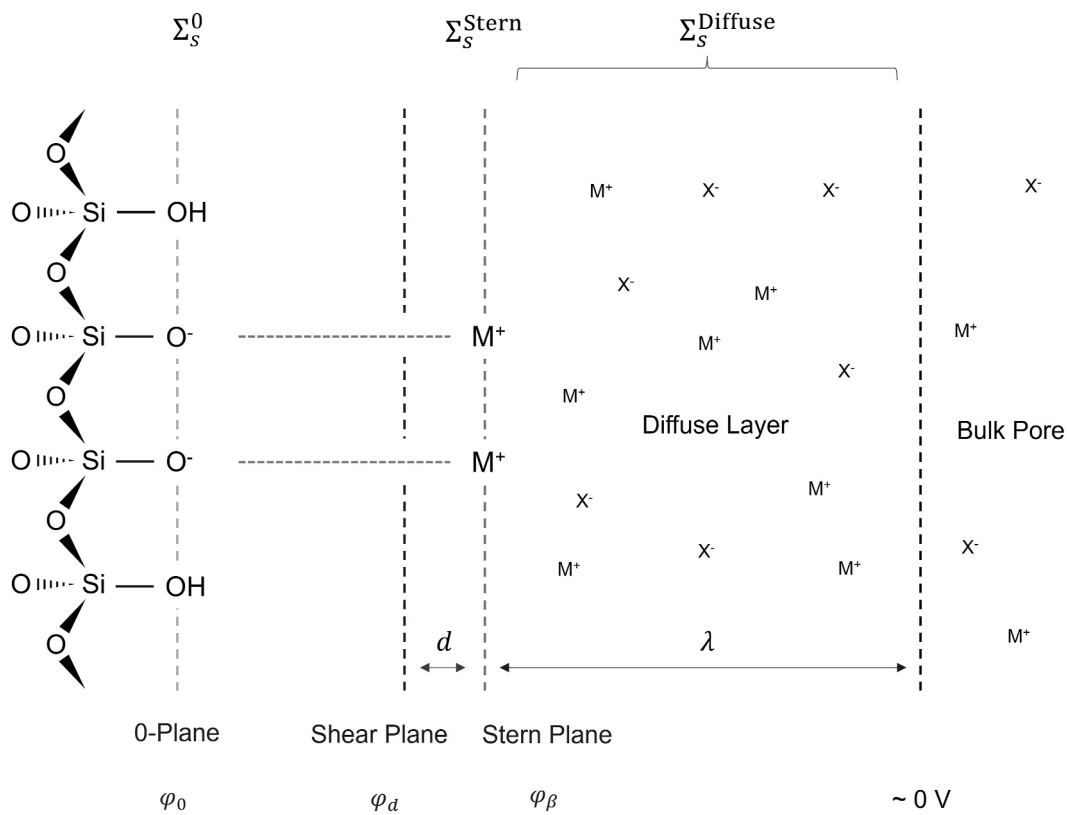

Figure 2. Sketch of the basic Stern model (BSM) developed by Leroy et al. (2013, 2022).

$$Q_0 = -e(\Gamma_{>SiO^-} + \Gamma_{>SiO^--M^+}), \tag{6}$$

$$Q_\beta = e\Gamma_{>SiO^--M^+}, \tag{7}$$

$$Q_S = \sqrt{8000\varepsilon_w k_B T N_A I}\sinh\left(-\frac{e\varphi_\beta}{2k_B T}\right), \tag{8}$$

$$Q_0 + Q_\beta + Q_S = 0, \tag{9}$$

$$\varphi_0 - \varphi_\beta = \frac{Q_0}{C_1}, \tag{10}$$

$$\varphi_d = \varphi_\beta - (\varphi_\beta - \varphi_0)\frac{C_1}{\varepsilon_1}d, \tag{11}$$

where Q_0, Q_β, and Q_S are charge densities (in C m^{-2}) of the mineral surface (0-plane), Stern layer, and diffuse layer, respectively. φ_0, φ_β, and φ_d are electrical potentials (in V) at 0-plane, Stern plane (i.e., outer Helmholtz plane), and shear plane, respectively. $\Gamma_{>SiO^-}$ and $\Gamma_{>SiO^--M^+}$ are surface site densities (in sites m^{-2}) of SiO^- at 0-plane and cation (M^+) at Stern plane (">" stands for the crystalline framework), respectively. k_B is the Boltzmann constant (1.381×10^{-23} J K^{-1}), N_A is the Avogadro number (6.022×10^{23} mol^{-1}), ε_w is the dielectric permittivity of pore water (in F m^{-1}), and I is the ionic strength (in mol L^{-1}). C_1 and ε_1 are the capacitance (in F m^{-2}) and dielectric permittivity (in F m^{-1}) of the Stern layer, respectively, and d is the distance (in m) between the Stern plane and the shear plane. $\Gamma_{>SiO^-}$ and $\Gamma_{>SiO^--M^+}$ in Equations 6 and 7 are calculated under the following thermodynamic equilibrium condition:

$$\Gamma_{>SiO^-} = \frac{\Gamma_S}{A}, \tag{12}$$

$$\Gamma_{>SiO^--M^+} = \frac{\Gamma_S}{A}K_{M^+}a^w_{M^+}\exp\left(-\frac{e\varphi_\beta}{k_B T}\right), \tag{13}$$

with

$$A = 1 + K_2 a^w_{H^+}\exp\left(-\frac{e\varphi_0}{k_B T}\right) + K_{M^+}a^w_{M^+}\exp\left(-\frac{e\varphi_\beta}{k_B T}\right), \tag{14}$$

where Γ_S is the total surface site density (in sites m^{-2}), a^w_i is the activity of species i in pore water, and K_2 and K_{M^+} are equilibrium constants defined for each reaction of

$$>SiO^- + H^+ \Leftrightarrow\ >SiOH, \quad K_2, \tag{15}$$

$$>SiO^- + M^+ \Leftrightarrow\ >SiO^- - M^+, \quad K_{M^+}. \tag{16}$$

These equilibrium constants at temperature T (K) are calculated using the following equation of chemical equilibrium at isothermal condition:

$$\Delta G^0_f(T) = -RTlnK, \tag{17}$$

where $\Delta G^0_f(T)$ is the standard Gibbs energy (J mol^{-1}) of formation at 0.1 MPa, R is the molar gas constant (8.314 J K^{-1} mol^{-1}), and K is the equilibrium constant.

The surface reaction of (15) occurs at the 0-plane and that of (16) occurs at the Stern plane. Equations 6–10 were solved for the variables of Q_0, Q_β, Q_S, φ_0, and φ_β using the Newton–Raphson method. Table 3 shows the parameter values in Equations 6–11 used in this study, which were derived from Leroy et al. (2022). It should be noted that $\Delta G^0_f(T)$, C_1, and ε_1 were assumed to be constants obtained at 20–25°C and approximately 0.1 MPa.

Table 3
Parameter Values of BSM in Equations 6–11

Symbols	Values
Γ_S (sites m^{-2})	4.6×10^{18}
K_2[a]	2.04×10^{7}
K_{Na^+}[a]	3.80
C_1 (F m^{-2})	3.43
ε_1 (F m^{-1})	3.81×10^{-10}
d (m)	2.0×10^{-11}

[a]Values are equilibrium constant at 298.15 K. The values at a given temperature T (K) are calculated by multiplying them by exp(298.15/T) based on Equation 17.

Although these values can depend on temperature and pressure (e.g., Alizadeh & Wang, 2020), to our knowledge, no studies have investigated these values under the conditions covered in the present study (25–200°C and 0.1–5 MPa). Nevertheless, as discussed in Section 2.1.4, assuming them as constants allowed us to obtain reasonable temperature dependencies at high pressure (3.45 MPa). Therefore, we decided to use these assumptions.

The specific surface conductance of the quartz was then calculated using the following equation (Leroy et al., 2013):

$$\Sigma_s = \Sigma_s^0 + \Sigma_s^{\text{Stern}} + \Sigma_s^{\text{Diffuse}}, \tag{18}$$

where Σ_s is the specific surface conductance, representing the increments from the conductance of pore water at the surface (in S). Σ_s^0 is the conductance due to the transport of protons on the surface and is set to a constant of 1.53 nS (Leroy et al., 2013), Σ_s^{Stern} is the conductance of the Stern layer (in S), and $\Sigma_s^{\text{Diffuse}}$ is the conductance of the diffuse layer (in S).

Σ_s^{Stern} was calculated using:

$$\Sigma_s^{\text{Stern}} = e\beta_{\text{M}^+}^S \Gamma_{>\text{SiO}^-\text{M}^+}, \tag{19}$$

where $\beta_{\text{M}^+}^S$ is the mobility of cation M^+ in the Stern layer (in m^2 s^{-1} V^{-1}). The mobility of sodium ions in the Stern layer was calculated using an empirical equation based on the results of molecular dynamics (MD) simulations by Zhang et al. (2011):

$$\beta_{\text{Na}^+}^S = 0.1\beta_{\text{Na}^+}^w \exp(-7.0m - 0.105), \tag{20}$$

where $\beta_{\text{Na}^+}^w$ is the mobility of sodium ion in pore water. $\Sigma_s^{\text{Diffuse}}$ was then calculated using:

$$\Sigma_s^{\text{Diffuse}} = 2000eN_A\lambda\sum_i \left(\beta_i^w + \frac{2\epsilon_w k_B T}{v_i e\eta_w}\right) c_i^w \left\{\exp\left(\frac{-v_i e\varphi_d}{2k_B T}\right) - 1\right\}, \tag{21}$$

where v_i is the valence of ion i, c_i^w is the molarity of ion i in pore water (in mol L^{-1}), η_w is the dynamic viscosity of pore water (in Pa s), and λ is the Debye length (in m) calculated as follows:

$$\lambda = \sqrt{\frac{\epsilon_w k_B T}{2000e^2 N_A I}}. \tag{22}$$

The right-hand side of Equation 21 is the sum of the electro-osmotic conductance derived from the Stokes equation and electromigration conductance, which is calculated based on the assumption that the ion mobility in the diffuse layer is equal to that in the pore water (Revil & Glover, 1997). It is worth mentioning that Equations 8, 19–21 implicitly assume that the Debye length is smaller than the local radius of the curvature of the mineral surface and the pore size (Revil & Glover, 1997). Therefore, the unit element of quartz and aqueous NaCl solution should be significantly larger than approximately 1–10 nm, which is the order of the Debye length calculated under 20°C–200°C and 10^{-4}–5 mol kg^{-1} covered in this study.

The specific surface conductance calculated by Equations 18–22 agreed well with the experimental data of Watillon and de Backer (1970) and Sonnefeld et al. (2001) measured at 20°C–25°C (Figure 3) within the order of 10^{-8} S, as highlighted in previous studies (Leroy et al., 2013; Revil & Glover, 1998). It is worth noting that these studies measured the surface conductance of the amorphous silica, which might differ from the surface conductance of quartz calculated in this study. However, the zeta potential of amorphous silica and that of quartz are close at low salinity (< difference 5 mV) (Leroy et al., 2013, 2022; Walker & Glover, 2018); therefore, both

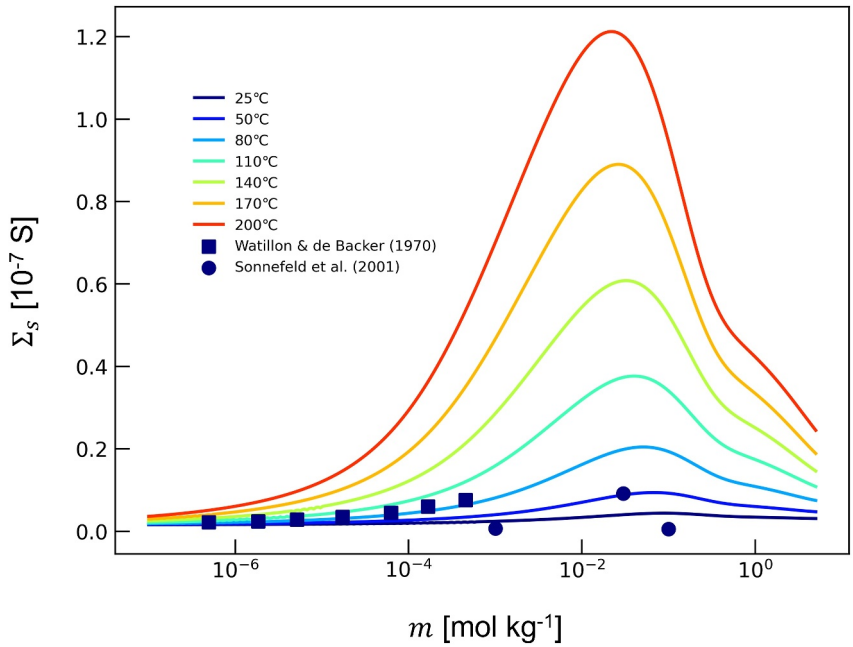

Figure 3. Specific surface conductance of quartz as a function of molality. Colors indicate temperature (in °C). The squares represent the experimental data (KNO_3(aq), T_c~20–25°C) as measured by Watillon and de Backer (1970). Referring to Revil and Glover (1998), the conductivity of the aqueous solution was converted to molality, assuming that molarity and molality are equal in such a dilute solution. The circles represent the specific surface conductance (NaCl(aq), T_c = 25°C) calculated from the Dukhin number measured by Sonnefeld et al. (2001). This study only explicitly showed the Dukhin number obtained at 10^{-3} M NaCl; thus, we compiled those values from Leroy et al. (2013). When calculating the surface conductivity from the Dukhin number, the effective radius was set to 150 nm based on Leroy et al. (2013).

surface conductances are deemed to be close as well. The smaller calculated values than the experimental data of Watillon and de Backer (1970) (squares in Figure 3) may be mainly due to (1) the mobility of Na^+, which is approximately 1.5 times smaller than that of K^+ when the solution is dilute (e.g., Roger et al., 2009) and (2) differences in the parameter values of BSM (Table 3). The inconsistencies with the experimental data of Sonnefeld et al. (2001) (circles in Figure 3) may be due to the inadequacy of the equation used to evaluate the experimental data, as discussed in Leroy et al. (2013). Furthermore, the conductivity of the aqueous NaCl solution (Equation 1) used for the conversion from the Dukhin number to specific surface conductance may differ from the conductivity of the solution in the experimental system. Although it remains unconfirmed whether the surface conductance agrees with experimental data above 10^{-1} M, this model can reproduce the zeta potential that Walker and Glover (2018) measured over varied salt concentrations (~10^{-4}–5.5 M NaCl). Therefore, the specific surface conductance is deemed accurate at high salt concentrations as long as Equations 18–22 hold. The temperature dependence of the specific surface conductance of quartz will be discussed in Section 2.1.4.

2.1.3. Smectite

Smectite is a 2:1 phyllosilicate composed of tetrahedra–octahedra–tetrahedra (TOT) layers and interlayers. Al^{3+} in the octahedral sheet and Si^{4+} in the tetrahedral sheet are partly replaced by Mg^{2+} and Al^{3+} or Mg^{2+}, respectively, attracting cations to the interlayer to compensate for the excess negative charges. This study considers saturated conditions alone. Thus, the interlayer was assumed to be filled with an aqueous NaCl solution. The electrochemical properties of the Na-smectite interlayer were calculated using the 1-pK triple layer model (TLM) developed by Gonçalvès et al. (2007) (Figure 4):

$$Q_0 = \frac{e}{2}\left[\frac{\Gamma_1^0}{A'}\left\{\frac{a_{H^+}^w}{K_1'}\exp\left(\frac{-e\varphi_0}{k_BT}\right)-1\right\}+\frac{\Gamma_2^0}{B'}\left\{\frac{a_{H^+}^w}{K_2'}\exp\left(\frac{-e\varphi_0}{k_BT}\right)-1\right\}-2\Gamma_3^0\right]+Q_i, \quad (23)$$

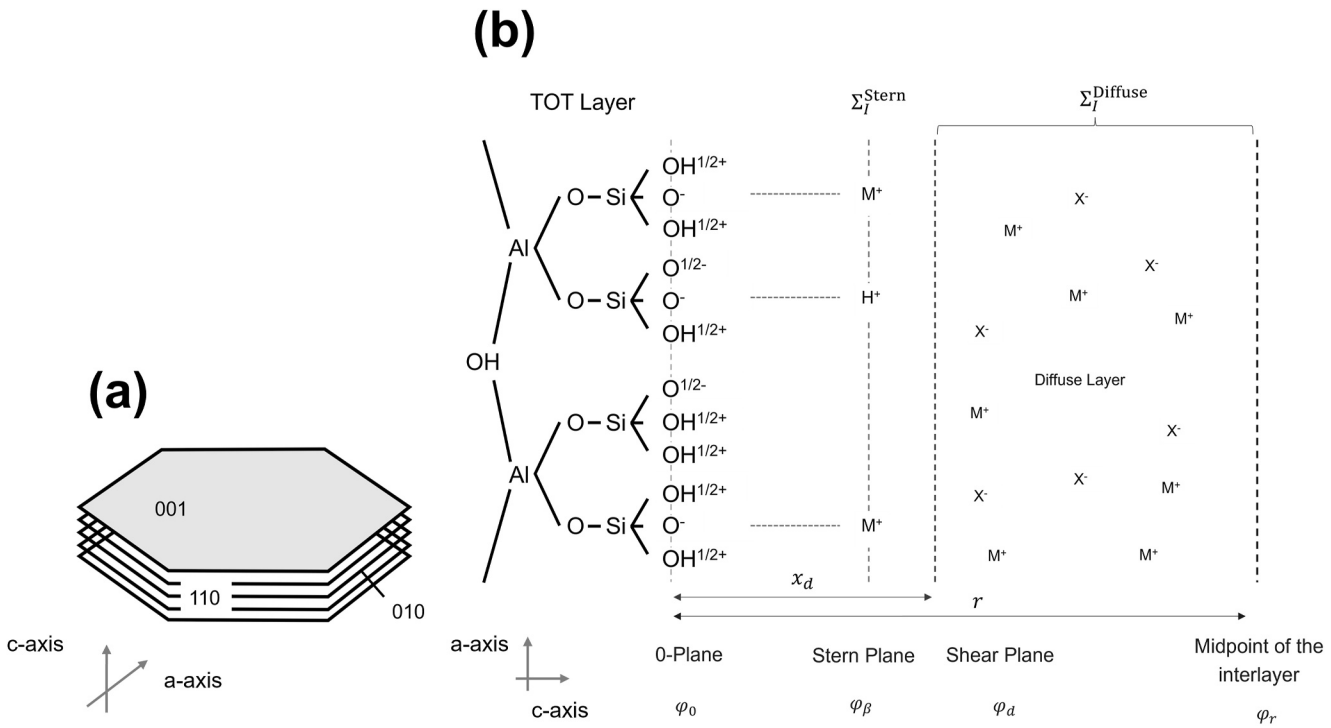

Figure 4. Schematic illustration of smectite's structure. (a) Smectite particles (adapted from Figure 1 in Leroy & Revil, 2004). (b) Sketch of the TLM developed by Gonçalvès et al. (2007). The >OH denotes the hydroxyl group located at the center of the six-membered ring of oxygens.

$$Q_\beta = e\frac{\Gamma_3^0}{C'}\left(\frac{a_{H^+}^w}{K_3'} + \frac{a_{Na^+}^w}{K_4'}\right)\exp\left(\frac{-e\varphi_\beta}{k_BT}\right), \tag{24}$$

$$Q_0 + Q_\beta + Q_S = 0, \tag{25}$$

$$\varphi_0 - \varphi_\beta = \frac{Q_0}{C_1'}, \tag{26}$$

$$\varphi_\beta - \varphi_d = -\frac{Q_S}{C_2'}, \tag{27}$$

$$Q_S = 2\sqrt{1000N_Ac^wk_BT\varepsilon_w\left\{\cosh\left(\frac{e\varphi_d}{k_BT}\right) - \cosh\left(\frac{e\varphi_r}{k_BT}\right)\right\}}, \tag{28}$$

$$\varphi_d = \varphi_r + \frac{10^3eN_Ac^w}{\varepsilon_w}\sinh\left(\frac{e\varphi_r}{k_BT}\right)(x_d - r)^2 + \frac{10^6e^3{N_A}^2c^{w2}}{12{\varepsilon_w}^2k_BT}\sinh\left(\frac{2e\varphi_r}{k_BT}\right)(x_d - r)^4, \tag{29}$$

with

$$A' = 1 + \frac{a_{\mathrm{H}^+}^w}{K_1'}\exp\left(\frac{-e\varphi_0}{k_BT}\right), \tag{30}$$

$$B' = 1 + \frac{a_{\mathrm{H}^+}^w}{K_2'}\exp\left(\frac{-e\varphi_0}{k_BT}\right), \tag{31}$$

$$C' = 1 + \left(\frac{a_{\mathrm{H}^+}^w}{K_3'} + \frac{a_{\mathrm{Na}^+}^w}{K_4'}\right)\exp\left(\frac{-e\varphi_\beta}{k_BT}\right), \tag{32}$$

Table 4
TLM Parameter Values for Calculating the Electrochemical Properties of the Interlayer and EDL at the Interface of Solid and Macropore Water

Symbols	Values	
	Interlayer	EDL facing bulk pore
Γ_1^0 (sites m^{-2})	0.0	0.0
Γ_2^0 (sites m^{-2})	5.5×10^{18}	5.5×10^{18}
Γ_3^0 (sites m^{-2})	5.5×10^{18}	5.5×10^{18}
Q_i (C m^{-2})	−0.16	−0.44
K_1' [a]	1.0×10^{-10}	1.0×10^{-10}
K_2' [a]	1.3×10^{-6}	1.3×10^{-6}
K_3' [a]	1.0×10^{-2}	1.0×10^{-2}
K_4' [a]	0.95	0.50
C_1' (F m^{-2})	2.1	0.93
C_2' (F m^{-2})	0.55	2.56

[a]Values are equilibrium constants at 298.15 K. The values at a given temperature T (K) are calculated by multiplying them with exp(298.15/T) based on Equation 17.

Table 5
Relationship Between the Thickness of the Interlayer (2r) and the Distance From the Basal Surface to the Shear Plane (xd)

2r (in Å)	x_d (in Å)
9.40	2.08
12.3	2.41
15.2	4.21
18.4	4.18
21.6	4.22

Note. x_d was linearly interpolated with 2r.

where Γ_1^0, Γ_2^0, and Γ_3^0 are surface site densities (in sites m^{-2}) of aluminol, sianol, and >Al-O-Si-O, respectively. Q_i is half of the permanent charge density (in C m^{-2}) and C_1' and C_2' are the capacitances of the inner and outer parts of the Stern layer (in F m^{-2}), respectively. c^w is the molarity (mol L^{-1}), φ_r is the electric potential at the midpoint of the interlayer (in V), r is the half thickness of the interlayer (in m), x_d is the distance between the centers of the oxygens in the siloxane surface and the shear plane (in m) (Figure 4), and K_1', K_2', K_3', and K_4' are the equilibrium constants defined for each surface reaction of

$$> \mathrm{AlOH_2^{\frac{1}{2}+}} \Leftrightarrow > \mathrm{AlOH^{\frac{1}{2}-}} + \mathrm{H^+}, \quad K_1', \tag{33}$$

$$> \mathrm{SiOH^{\frac{1}{2}+}} \Leftrightarrow > \mathrm{SiO^{\frac{1}{2}-}} + \mathrm{H^+}, \quad K_2', \tag{34}$$

$$> \mathrm{XH^0} \Leftrightarrow > \mathrm{X^-} + \mathrm{H^+}, \quad K_3', \tag{35}$$

$$> \mathrm{XNa^0} \Leftrightarrow > \mathrm{X^-} + \mathrm{Na^+}, \quad K_4', \tag{36}$$

where > X stands for the surface sites of >Al-O-Si-O. Equations 23–29 were solved for the variables of Q_0, Q_β, Q_S, φ_0, φ_β, φ_d, and φ_r using the Newton–Raphson method. The parameter values in Equations 23–32 were derived from Gonçalvès et al. (2007) (Table 4), whereas x_d was set as a variable depending on the layer thickness (i.e., 2r), based on the location of the peak number density of Na^+ computed by the MD simulation by Zhang et al. (2014) (Table 5). As with the case of quartz, the standard Gibbs energy of formation (Equation 17), along with C_1' and C_2', were assumed to be constants.

It is worth mentioning that Equations 23–36 were derived from Leroy and Revil (2004), who originally considered the basal (001) plane of phyllosilicate as inert (i.e., hydrophobic), and the surface reactions of (33)–(36) occur at the edges of the (110) and (010) planes. However, the MD simulations by Szczerba et al. (2020) revealed that the (001) plane is hydrophilic due to the cations attracted to the surface to satisfy electrical neutrality. Gonçalvès et al. (2007) accurately reproduced the measurement of swelling pressure decreasing as the interlayer thickens using Equations 23–36. In addition, the assumptions of the Poisson–Boltzmann distributions in Equations 28 and 29 find support in MD simulations (e.g., Tinnacher et al., 2016). Given these considerations, we deemed Equations 23–36 appropriate for calculating the electrochemical properties of the interlayer.

The conductance of the interlayer, Σ_{intra} (in S), was then obtained from the following equation, ignoring the contribution of protons (Leroy et al., 2015; Leroy & Revil, 2004):

$$\Sigma_{intra} = \Sigma_I^{\mathrm{Stern}} + \Sigma_I^{\mathrm{Diffuse}}, \tag{37}$$

where $\Sigma_I^{\mathrm{Stern}}$ is the conductance of the Stern layer (in S) and $\Sigma_I^{\mathrm{Diffuse}}$ is the conductance of the diffuse layer (in S). $\Sigma_I^{\mathrm{Stern}}$ was obtained from

$$\Sigma_I^{\mathrm{Stern}} = e\beta_{\mathrm{Na^+}}^{S'}\Gamma_{>\mathrm{X-Na^+}}, \tag{38}$$

with

$$\Gamma_{>\mathrm{X-Na^+}} = \frac{\Gamma_3^0}{C'}\frac{a_{\mathrm{Na^+}}^w}{K_4'}\exp\left(\frac{-e\varphi_\beta}{k_BT}\right), \tag{39}$$

where $\beta_{\mathrm{Na^+}}^{S'}$ is the mobility of the cation Na^+ on the Stern plane (in m^2 s^{-1} V^{-1}) and $\Gamma_{>\mathrm{X-Na^+}}$ is the surface density of the cation on the Stern plane (in sites m^{-2}). $\beta_{\mathrm{Na^+}}^{S'}$ was set to half of the mobility of the bulk pore water based on the MD simulation results (Bourg & Sposito, 2011; Tournassat et al., 2009; Zheng et al., 2023), that is,

$$\beta^{S'}_{Na^+} = 0.5\beta^{w}_{Na^+}. \quad (40)$$

$\Sigma_I^{\text{Diffuse}}$ was calculated using:

$$\Sigma_I^{\text{Diffuse}} = 1000eN_A \int_{x_d}^{r} \sum_i c_i^w \beta_i^I (x + x_d) \exp\left(\frac{-v_i\varphi(x)}{k_BT}\right) dx, \quad (41)$$

where $\varphi(x)$ is the potential (in V) at distance x from the shear plane (in m) and $\beta_i^I(x)$ is the mobility (in $m^2\ s^{-1}\ V^{-1}$) of ion i at the distance x. Here, $\varphi(x)$ is given by

$$\varphi(x) = \varphi_d \exp\left(-\frac{1}{r} ln\left(\frac{\varphi_d}{\varphi_r}\right) x\right), \quad (42)$$

and $\beta_i^I(x)$ is given based on the distributions of self-diffusion coefficients parallel to the TOT surface predicted by MD simulations (Bourg & Sposito, 2011):

$$\beta_i^I(x) = \beta_i^w \{1 - \exp(-1.4 \times 10^9 x)\}. \quad (43)$$

The mobility calculated using this equation is lower than that of the bulk solution, as it does not include the contribution of electro-osmosis.

If the TOT layer is parallel to an XY plane (i.e., the c-axis is parallel to the Z-axis) and the unit element has a cubic shape, the conductivity tensor can be expressed as follows:

$$\boldsymbol{\sigma}_{smectite} = \begin{bmatrix} \sigma_{XY} & 0 & 0 \\ 0 & \sigma_{XY} & 0 \\ 0 & 0 & \sigma_Z \end{bmatrix}, \quad (44)$$

where σ_{XY} and σ_Z are combined conductivity of the interlayer and TOT in parallel and series, respectively, and are calculated as

$$\sigma_{XY} = \frac{2r\sigma_r + d_{TOT}\sigma_{TOT}}{2r + d_{TOT}}, \quad (45)$$

$$\sigma_Z = \frac{2r + d_{TOT}}{\frac{2r}{\sigma_r} + \frac{d_{TOT}}{\sigma_{TOT}}}, \quad (46)$$

where σ_r is the conductivity of the interlayer (in S m^{-1}; $\sigma_r = \Sigma_{intra}/r$). d_{TOT} and σ_{TOT} are the thickness (in m) and conductivity (in S m^{-1}) of the TOT layer, respectively. As both the thicknesses of the tetrahedral and octahedral sheets are ~2.2 Å (Shirozu, 1988), d_{TOT} was set to 6.6 Å. From the discussion we had when assigning the conductivity of the solid phase of quartz, 10^{-12} S m^{-1} was also assinged to σ_{TOT}.

The electrochemical properties of the EDL that develops at the boundary between smectite and macropore water were calculated by solving Equations 23–27 and following Equation 47 for the variables of Q_0, Q_β, Q_S, φ_0, φ_β, and φ_d by the Newton–Raphson method. Here, Equation 47 is

$$Q_S = \sqrt{8000\varepsilon_w k_B T N_A I} \sinh\left(-\frac{e\varphi_d}{2k_BT}\right). \quad (47)$$

The parameter values (Table 4) were examined manually around the values reported by Leroy et al. (2015) to reproduce the zeta potentials of montmorillonite measured by Rasmusson et al. (1997). It is noteworthy that the charge density value of −0.44 C/m^2 is close to the upper limit of the experimental data (Revil et al., 1998). The

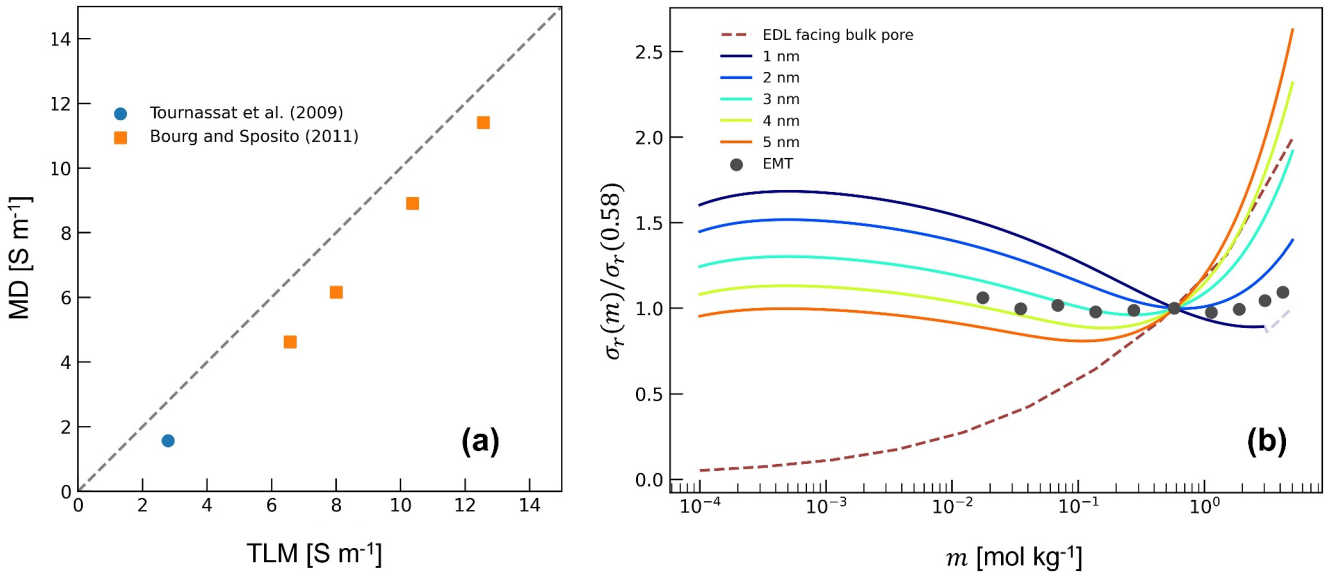

Figure 5. Comparison of interlayer conductivities of smectite based on the TLM with those estimated in previous studies. (a) Conductivity of the interlayer calculated from the results of the MD simulations (Bourg & Sposito, 2011; Tournassat et al., 2009) versus those calculated by TLM (the present study). The thickness of the interlayer and molarity refer to the values in Table 6, while the remaining parameters are from Tables 4 and 5. The self-diffusion coefficients of ions in the bulk water were computed by the mean spherical approximation (Roger et al., 2009). (b) Conductivity of the EDL in smectite as a function of molality, which is normalized by the EDL conductivity when the aqueous NaCl solution has a molality of 0.58 mol kg^{-1}. The solid lines indicate the conductivity of the interlayer, with colors representing the layer thickness (i.e., $2r$). The region with a molality over 3 mol kg^{-1} for a layer thickness of 1 nm had poor convergence due to overflow when solving Equations 23–29 with the Newton–Raphson method. The red dashed line shows the specific surface conductivity of the EDL that faces the bulk pore. The gray circles represent the results of the analysis by Revil et al. (1998) using drilled core samples.

specific surface conductance was then calculated in the same way as for quartz, using Equations 18, 19 and 21 substituting $\Sigma_s^0 = 0$ and $\beta_{Na^+}^S = 0.5\beta_{Na^+}^w$ (Leroy & Revil, 2004).

To our knowledge, no direct measurement data exist for the EDL conductivity of smectite. Therefore, to test the reliability of the TLM-based conductivity of interlayer water at an nm scale, we compared the conductivities obtained from Equation 37 with the MD simulation results, which investigate atom motions in the interlayer water at an Å scale, and with the effective medium theory (EMT), which estimates the EDL conductivity on a cm scale of the core sample.

The conductivities calculated from the distribution of the number densities and self-diffusion coefficients of interlayer cations and anions based on MD simulations (Bourg & Sposito, 2011; Tournassat et al., 2009) and those calculated using Equation 37 generally agreed within ~2.0 S m^{-1} (Figure 5a). The discrepancies between them may be due to (1) the different parameters of cation compositions and permanent charge densities (Tables 4 and 6); (2) the errors caused by the assumptions in the TLM applied for simplicity, such as the ion activity in the interlayer being equal to that of bulk water; and (3) the numerical errors in the MD simulations. The interlayer conductivities also aligned with the results of the EMT analysis by Revil et al. (1998) (Figure 5b herein). At low

Table 6
Parameter Values of MD Simulations (Bourg & Sposito, 2011; Tournassat et al., 2009)

Parameter	Tournassat et al. (2009)	Bourg and Sposito (2011)
Half of the permanent charge density (C m^{-2})	−0.058	−0.21
Interlayer cation	Only Na^+	Na^+ and Ca^{2+} [a]
Thickness of the interlayer (nm)	16.3[b]	5.8
Molarity (mol_c L^{-1})	0.1	0.34–1.83

Note. Both simulations were performed under conditions of 298 K and a constant gauge pressure of 0 Pa. [a]Ratio of the number densities of Na^+ and Ca^{2+} was 2:1 (i.e., the chemical equivalents were equal). [b]The thickness of the TOT layer was read from the graph as 6.9 Å.

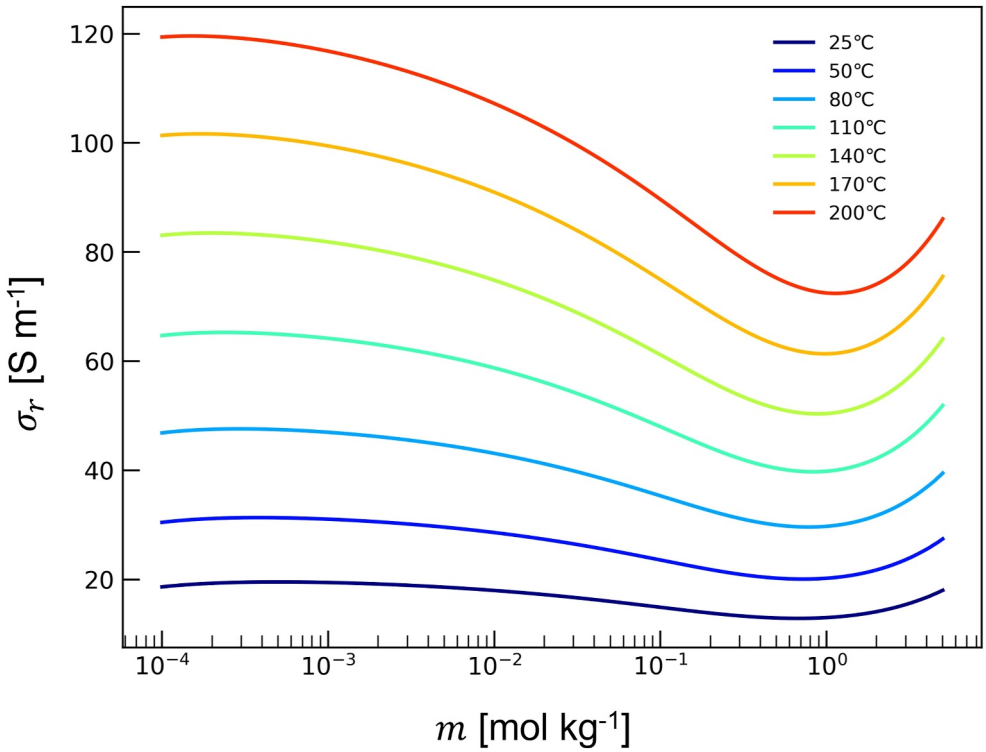

Figure 6. Conductivity of the smectite interlayer as a function of molality ($2r$ = 2 nm; pressure is 5 MPa). Colors indicate temperature (in °C).

salt concentrations (<~0.6 mol kg^{-1}), the analytical results from the EMT approached the 3–4 nm lines, whereas at higher salt concentrations, those results asymptotically approached the 1–2 nm lines. This shift may correspond to an osmotic expansion process in which the thickness of the smectite layer (i.e., d_{001}) decreases with increasing salt concentration (e.g., Svensson & Hansen, 2013). However, the conductivity of the EDL developing on the bulk pore disagreed with the results of the EMT analysis, which may be attributed to the concentration of the current flowing through the smectite in the interlayer (e.g., Leroy & Revil, 2009). The linear increase in interlayer conductivity with increasing temperature (Figure 6) will be discussed in Section 2.1.4.

2.1.4. Validity of the Temperature Dependence of Surface Conductivity

Although no direct measurement data of the surface conductivity of quartz and smectite covering the 20°C–200°C range exist, several previous studies have estimated the temperature dependence of EDL conductivity by applying empirical equations to bulk conductivity data measured over varied temperatures (25°C–200°C) and salinities (0.09–4.74 mol kg^{-1}) (Waxman & Thomas, 1974; Clavier et al., 1984; Sen & Goode, 1992; Revil et al., 1998). These studies predicted that the EDL conductivity increases linearly with increasing temperature, which aligns with the calculations in our study (Figure 7). In addition, the EDL conductivities predicted in these studies fell roughly between those of quartz and smectite calculated in our study. This is reasonable because the estimated EDL conductivities in previous studies represent the effective conductivities of pathways through (1) the surface of minerals with permanent charges, such as smectite; (2) those with only variable charges, such as quartz; and (3) aqueous NaCl solutions. Further quantitative comparisons were impossible because previous studies have not quantified clay minerals. However, based on the qualitative discussion above, we consider the temperature dependence of each component calculated in this study reliable. The close temperature dependences of the interlayer conductivity and the NaCl solution in the pore water align with the MD simulations, which revealed that the self-diffusion coefficients of Na^+ in the interlayer are about half of the bulk solution regardless of the temperature in 25°C–100°C (Zheng et al., 2023).

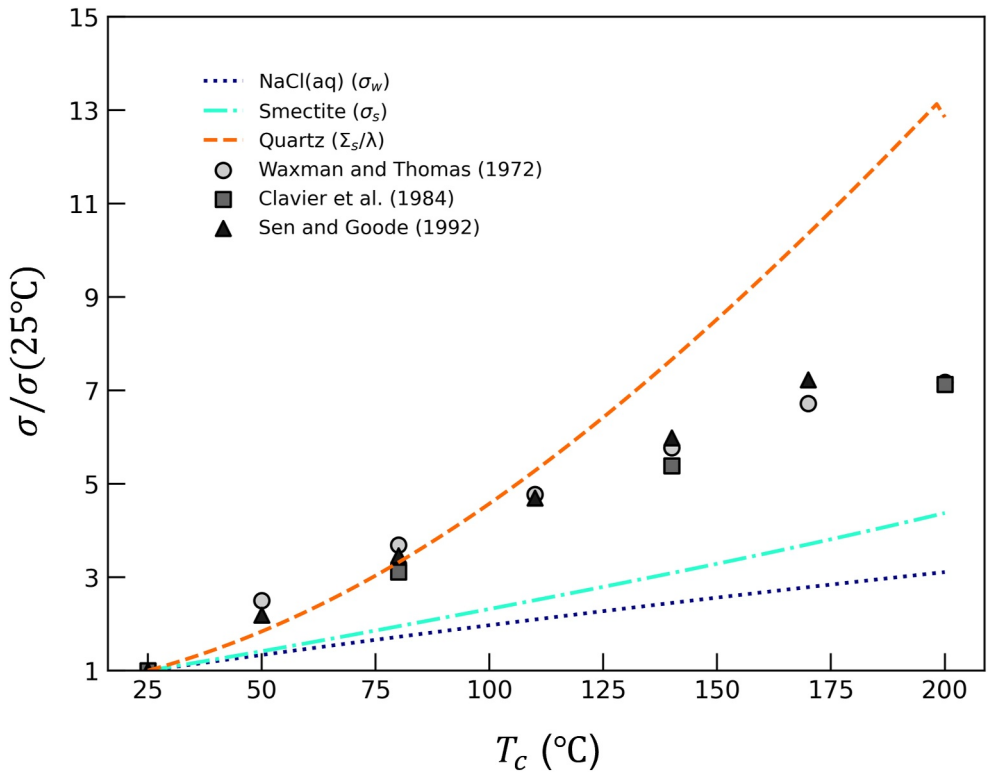

Figure 7. Normalized conductivity at 25°C as a function of temperature. The blue, green, and orange lines represent the conductivity of the aqueous NaCl solution, the interlayer of smectite, and the EDL on the quartz surface, respectively. The circles, squares, and rectangles correspond to data from Waxman and Thomas (1974), Clavier et al. (1984), and Sen and Goode (1992), respectively. These conductivities have been normalized to their values at 25°C. The temperature dependences of the surface conductivities estimated in previous studies are compiled from the mobilities multiplied by the surface charge densities. As these mobilities are major contributors to the bulk conductivities at low salinities, the conductivities of each component (lines) were calculated at 0.09 mol kg^{-1} (the lowest of the molalities covered by previous studies). The pore pressure was set to 3.45 MPa, which was the same as that in the experimental system.

2.2. Assignment of Components

The conductivity tensor of NaCl solution (i.e., pore space), quartz, and smectite calculated in Section 2.1 was assigned to the discretized model space using the following two methods:

1. Anisotropic assignment (Figure 8): Utilizing an anisotropic scaling factor, a randomly selected initial placement was spatially interpolated by ordinary kriging (e.g., Wackernagel, 1995). First, N_1 voxels were randomly selected from those yet to be assigned to scatter the voxels with conductive components (i.e., NaCl (aq) or smectite) throughout the model space without an end-to-end connection. It is important to note that quartz was assigned to the last remaining voxels instead of kriging. Here, N_1 is an integer approximately half of N_t, where N_t is a target number (integer) obtained by rounding the volume fraction of the component multiplied by the total number of voxels in the model space. Subsequently, those initially selected voxels were assigned probabilities in 0–1. These probabilities were interpolated on the location of the yet unassigned voxels through anisotropic ordinary kriging to ensure that the ratios of autocorrelation lengths on the Y- and *Z*-axes (i.e., axes without voltage) to the *X*-axis (i.e., axis for applying voltage) were proportional to constant *k*. The smaller the *k* value, the more conductive paths form in the *X*-axis and less in the Y- and *Z*-axes (Figure 8). Similar to the random assignment method described below, the distribution is uniquely determined once a random seed value is given. This method was employed in simulations when reproducing the bulk conductivity data from core samples in previous studies (Section 2.4), with rotation matrices being either fixed or randomly given.
2. Random assignment (Figure 9): The conductivity tensors were randomly assigned and rotated. The distribution of the components was determined by random sampling of the indices of voxels that had not yet been assigned. Rotation matrices were obtained for each element through QR decomposition of randomly generated

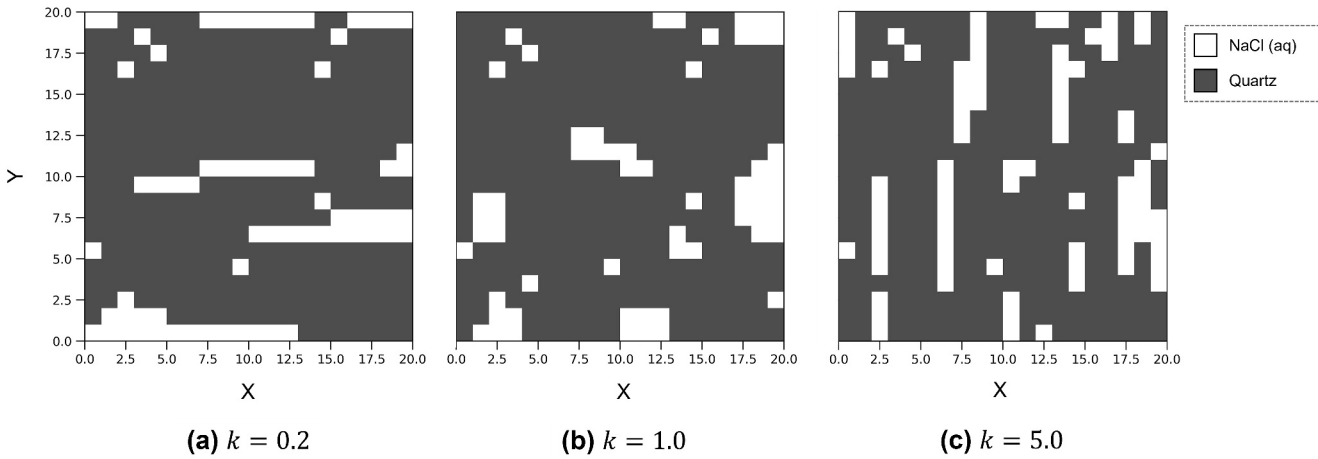

Figure 8. Examples of component daistributions realized by anisotropic ordinary kriging ($N_x = N_y = N_z = 20$). Cases with the anisotropic ratio for NaCl solution of (a) $k = 0.2$, (b) $k = 1.0$, and (c) $k = 5.0$. The pore volume fraction (i.e., the volume fraction of NaCl solution in the entire volume of the model space) is 0.2 for all cases here, and smectite is not shown in this figure for clarity.

3×3 matrices using uniformly distributed random numbers. This method was used to investigate bulk conductivity dependence on various petrophysical conditions, such as temperature, salinity, or pore volume fraction (Section 2.4).

2.3. Finite Element Method

After the assignment of components to the gridded model space, the electric potential distribution was computed using FEM to minimize the resistive loss in the rock. We added the functionality of Ventcel's boundary condition to the computational code developed by Garboczi (1998) to calculate the resistive loss associated with surface conduction. Separate element stiffness matrices were prepared for both volume and surface elements. For the cubic volume element, the stiffness matrix is defined by the following equation:

$$D^v_{rs} = \int_0^1 \int_0^1 \int_0^1 \left\{ \sum_p \sum_q \frac{\partial \phi_r}{\partial p} \sigma_{pq} \frac{\partial \phi_s}{\partial q} \right\} dxdydz, \tag{48}$$

where D^v_{rs} is the r, s entry in 8×8 stiffness matrix of $\boldsymbol{D}^v$ (r and s denote the indices of vertices in Figure 10a), σ_{pq} is the p, q entry of the conductivity tensor in $\boldsymbol{\sigma}$ (p and q represent the indices of axes where one corresponds to the X-

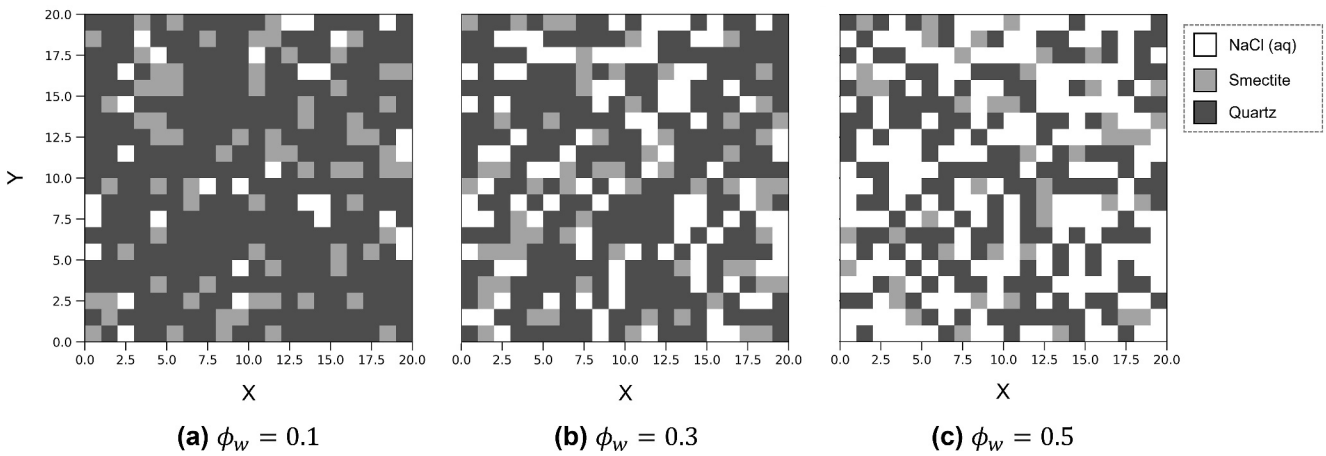

Figure 9. Distribution of randomly assigned components ($N_x = N_y = N_z = 20$) with a volume fraction of NaCl solution (ϕ_w) as (a) 0.1, (b) 0.3, and (c) 0.5. The volume fraction of smectite for the solid phase (not the entire model volume) is 0.1 for all cases here.

Table 7
Linear Shape Functions at the Vertices of Cubic Elements

ϕ_i	Shape functions
ϕ_1	$(1-x)\,(1-y)\,(1-z)$
ϕ_2	$x(1-y)\,(1-z)$
ϕ_3	$xy(1-z)$
ϕ_4	$(1-x)y(1-z)$
ϕ_5	$(1-x)\,(1-y)z$
ϕ_6	$x(1-y)z$
ϕ_7	xyz
ϕ_8	$(1-x)yz$

axis, two to the Y-axis, and three to the Z-axis, respectively), and ϕ_i is the linear shape function defined at vertices i of a cubic element (Table 7 and Figure 10a). The integral interval was set to 0–1 for simplicity because the bulk conductivity obtained in this study is independent of the scale due to the periodic boundary condition mentioned later. Equation 48 can be accurately solved using Simpson's rule (Garboczi, 1998). Subsequently, the resistive loss (in W) in each volume element is calculated as follows:

$$E_n^v = \frac{1}{2}\boldsymbol{u}_v^T \boldsymbol{D}^v \boldsymbol{u}_v, \tag{49}$$

where $\boldsymbol{u}_v$ is the 8×1 column vector containing electric potentials at the vertices (in V) of the cubic element.

Similarly, the surface stiffness matrix on the solid–liquid boundary is defined as

$$D^{s}_{r's'} = \frac{\Sigma_s}{d}\int_{\Omega}\left\{\sum_{p'}\sum_{q'}\frac{\partial\phi_{r'}}{\partial p'}\frac{\partial\phi_{s'}}{\partial q'}\right\}d\Omega, \tag{50}$$

where $D^s_{r's'}$ is the r', s' entry in the 4×4 stiffness matrix of $\boldsymbol{D}^s$ (r' and s' denote the indices of vertices in Figure 10b), Σ_s is the specific surface conductance (in S) of the EDL developed at the solid–liquid boundary calculated using Equation 18, d is the edge length of the cube (in m), and p' and q' denote the indices of axes on the surface boundary Ω (Table 8 and Figure 10b). d should be much larger than the Debye length (1–10 nm in this study) in order to qualify the following two conditions: (1) the thin and flat layer assumption in the BSM (Leroy et al., 2013, 2022) and the TLM (Leroy & Revil, 2004) and (2) the condition required by the FEM that the EDL is thin enough compared to the volume elements. The energy generated on the surface per unit time (in W) is calculated as follows:

$$E_n^s = \frac{1}{2}\boldsymbol{u}_s^T \boldsymbol{D}^s \boldsymbol{u}_s, \tag{51}$$

where $\boldsymbol{u}_s$ is the 4×1 column vector containing electric potentials at the vertices (in V) of each square element on the surface.

Once the stiffness matrix for each element has been calculated, the total resistive loss is calculated using the following equation (Garboczi, 1998):

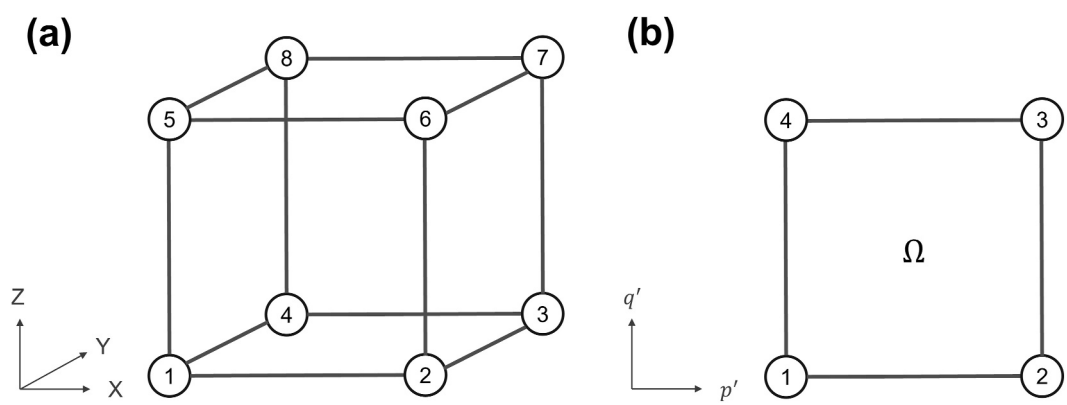

Figure 10. Indices of vertices. (a) Cubic element. (b) Surface element on the solid–liquid boundary.

Table 8
Linear Shape Functions at the Vertices of Square Elements on the Surface

ϕ_i	Shape functions
ϕ_1	$(1-p')(1-q')$
ϕ_2	$p'(1-q')$
ϕ_3	$(1-p')q'$
ϕ_4	$p'q'$

$$E = \frac{1}{2}\boldsymbol{u}^T\boldsymbol{A}\boldsymbol{u} + \boldsymbol{b}\cdot\boldsymbol{u} + c, \tag{52}$$

where $\boldsymbol{u}$ is the column vector containing electric potentials (in V) at every vertex, $\boldsymbol{A}$ is the global stiffness matrix built from $\boldsymbol{D}^v$ and $\boldsymbol{D}^s$ of all elements, and $\boldsymbol{b}$ and c are constants associated with the periodic boundary condition. E was minimized using the conjugate gradient method to obtain the optimum distribution of the potential $\boldsymbol{u}$. Finally, the bulk conductivity is calculated using the following equation:

$$\sigma_p = \frac{\langle i_p \rangle L_p}{\Delta V_p}, \tag{53}$$

where subscript p denotes the axis index, σ_p is the bulk conductivity, i_p is a vector containing the current density in each element (A m^{-2}) calculated from the potential $\boldsymbol{u}$, conductivity tensors, and specific conductance on the solid–liquid boundaries ($\langle\bullet\rangle$ denotes an average), ΔV_p is the voltage applied to the system (in V), and L_p is the length of the computational domain (in m). The simulated and theoretical bulk conductivities of rocks with layered quartz and NaCl solutions agreed within a relative error of 10^{-15} in the ranges of 20°C–200°C and 10^{-4}–5 mol kg^{-1} (pore pressure was set to be 5 MPa, and other conditions are listed in Table 9).

2.4. Simulation Conditions

All simulations were performed using the parameter settings listed in Table 9. It should be noted that we did not investigate the off-diagonal elements in the bulk-conductivity tensor as they fall beyond the scope of this study.

First, we tested the simulator's ability to reproduce core sample data from Waxman and Smits (1968) and Lévy et al. (2018), in which we performed simulations under the conditions listed in Table 10. Here, the mass fraction of smectite quantified by XRD in Lévy et al. (2018) was converted to a volume fraction using the average density of solid grains measured in the same core samples and the hydrated smectite's average density at 2.3 g cm^{-3}, which was assumed in their study. Meanwhile, as the smectite content was not quantified in Waxman and Smits (1968), the following equation proposed by Lévy et al. (2018) was applied to convert the surface charge density to the volume fraction of smectite:

$$X_{smec} = \frac{Q_v \phi}{202(1-\phi)}, \tag{54}$$

where X_{smec} is the volume fraction of smectite in the solid phase, Q_v is the excess of charge per unit pore volume (C cm^{-3}), and ϕ is the effective porosity. The effective porosity measured by Waxman and Smits (1968) and Lévy et al. (2018) may include the microporosity of the smectite interlayer; thus, the following equation was introduced to calculate the volume fraction of the macropore:

$$\phi_w = \frac{\phi - \phi_{smec}^{sol}}{1 - \phi_{smec}^{sol}}, \tag{55}$$

with

$$\phi_{smec}^{sol} = \frac{2rX_{smec}}{2r + d_{TOT}}, \tag{56}$$

where ϕ_w is the volume fraction of macropore and ϕ_{smec}^{sol} is the volume fraction of the smectite interlayer in the solid phase. Equation 55 was derived by equating the sum of the microporosity in smectite ($= [1-\phi_w]\phi_{smec}^{sol}$) and macroporosity ($\phi_w$) to the effective porosity (ϕ). The other temperature and salinity properties were set to the values provided in the aforementioned

Table 9
Parameter Values Commonly Used in the Simulations

Parameters	Values
Grid numbers (N_x,N_y,N_z)	20, 20, 20
Edge length of a cubic cell	1.0 μm
Voltages (V_x,V_y,V_z, in V)	20, 20, 20
Convergence criteria of the CG method[a]	8.0×10^{-13}
pH	7.0

[a]Criteria for the squared value of the L2 norm of the gradient vector $\frac{\partial E}{\partial \boldsymbol{u}}$.

Table 10
Experimental Conditions of the Core Samples

	Core IDs					
Symbols	WS26	L22	L24a	L31	L96	L113
T_c (in °C)	25.0	22.0	22.0	22.0	22.0	22.0
m (in mol kg^{-1})	1.7×10^{-2}–5.6	1.5×10^{-2}–0.64	1.5×10^{-2}–0.64	4.7×10^{-4}–1.6	1.5×10^{-3}–1.6	7.8×10^{-3}–1.6
P (in MPa)	0.1	0.1	0.1	0.1	0.1	0.1
ϕ	0.229	0.139	0.222	0.236	0.279	0.099
X_{smec}	0.209	0.177	0.324	0.242	0.331	0.111
N_{seed}	100	100	100	100	100	100

Note. The core IDs are based on those listed in previous studies (Lévy et al., 2018; Waxman & Smits, 1968). WS26 is from Waxman and Smits (1968), and the others are from Lévy et al. (2018). N_{seed} denotes the number of random seeds in our simulations.

papers. As the pore pressure was not specified in Waxman and Smits (1968) and Lévy et al. (2018), we assumed an atmospheric pressure of 0.1 MPa in our simulations. A voltage of 20 V was applied only on the X-axis and null on the other axes to make the condition similar to that in the laboratory experimental system. The thickness of the interlayer ($2r$), anisotropic ratio (k) of each material type, and rotation angles (θ) of the conductivity tensor of smectite around the Y-axis (conductivity tensors shown in Equations 2, 5 and 44 are defined at $\theta = 0°$) were searched for unknown parameters by trial and error. Owing to limited computational resources, we did not confirm the uniqueness of the solution (i.e., whether a global minimum exists). The bulk conductivity was computed from 100 different distributions generated by anisotropic kriging based on the corresponding 100 random seeds to estimate the variance of the simulations.

Second, we investigated the dependence of the bulk conductivity of smectite-bearing rocks on temperature, salinity, porosity, and smectite content. The simulation conditions are listed in Table 11. To accurately calculate the electrochemical properties of the interlayer, its thickness (i.e., $2r$) was set to 2 nm, allowing the TLM to reproduce the experimental data of osmotic pressure (Gonçalvès et al., 2007) and EMT analysis (Revil et al., 1998, Figure 5b herein). The pore pressure was fixed at 5 MPa, corresponding to the hydrostatic pressure at a depth of 500 m, where smectites are abundant in geothermal fields (e.g., Àrnason et al., 2000). For each condition, we computed the bulk conductivity from 10 different random distributions based on the corresponding random seeds to evaluate simulation variance. Furthermore, the empirical and theoretical models proposed in seven previous studies (Archie, 1942; Wyllie & Southwick, 1954; Waxman & Thomas, 1974; Bussian, 1983; Clavier et al., 1984; Sen & Goode, 1992; Qi & Wu, 2022) were fitted to our simulation results using the Levenberg–Marquardt method implemented by *the lmfit* package (Newville et al., 2023). The inverse of the square common logarithm of the variance calculated from 30 pieces of simulated data (10 random seeds × 3 axes) was employed as weights in the curve fitting.

Table 11
Simulation Conditions Under Which the Dependence of Bulk Conductivity on Petrophysical Properties was Studied

Symbols	Values
T_c (in °C)	20–200
m (in mol kg^{-1})	10^{-4}–5
ϕ_w	0–1
X_{smec}	0–1
P (in MPa)	5
$2r$ (in nm)	2
N_{seed}	10

Note. N_{seed} denotes the number of random seeds in the simulations.

3. Results and Discussion

3.1. Comparison With Experimental Data

The best-fitted geometrical parameters of the core samples, obtained by comparing the experimental data with our simulations, are listed in Table 12. Overall, the simulator reproduced the molality dependence of the experimental data within or close to the standard deviations derived from the randomness of the initial distribution in the anisotropic arrangement of components (Figure 11). For WS26, we reproduced the reported conductivity by giving a random distribution and angle of smectite (Table 12). Given that WS26 was collected from a depth of 982 m in a Tertiary horizon, burial consolidation might have contributed to forming a smectite's preferred orientation in the actual core sample parallel to the bedding plane (e.g., Kawamura, 2010). However, as Bowles (1968) reported random smectite

Table 12
Optimized Parameters.

Symbols	Core IDs					
	WS26	L22	L24a	L31	L96	L113
$2r$ (in nm)	2.0–4.0[a]	1.3	1.1	2.0	2.0	0.8
k_{smec}	R	0.5	5.0	5.0	5.0	0.6
$k_{\mathrm{NaCl(aq)}}$	0.7	R	R	R	R	R
θ_{smec}(°)	R	20.0	0.0	0.0	0.0	0.0

Note. k_{smec} and $k_{\mathrm{NaCl(aq)}}$ are anisotropic ratios of smectite and NaCl solution, respectively, θ_{smec} is the rotation angle of the tensor of smectite (in degree), and "R" denotes random settings under a given random seed. [a]$2r$ decreases linearly (4.0–2.0 nm) with increasing molality (1.7×10^{-2}–5.6 mol kg^{-1}). This setting is based on the analysis in Section 2.1.3 (Figure 5b).

distributions in the Gulf of Mexico even in high-pressure sedimentary environments (>33 MPa), we eventually opted for the random setting for k_{smec} and θ_{smec}. The other cores, L22–L113, were collected from depths of 131–582 m in the Krafla geothermal area, Iceland (Lévy et al., 2018; Scott et al., 2023). Due to the fact that these plugs were cored perpendicularly to the vertical core from the original drilling on-site, conductivities were overall measured along the horizontal plane (note that a significant part of smectite precipitation in altered volcanic rocks happens in fractures, which are not necessarily parallel to the bedding plane). Therefore, the low θ_{smec} of L22–L113 (Table 12) indicates that the TOT plane of the smectite may have been parallel to a horizontal direction, close to the bedding plane. These angles may be related to regional ground deformation in the Krafla area because particles with large aspect ratios, such as smectite, tend to rotate in response to the magnitude and anisotropy of the strain rate (e.g., Masuda et al., 1995). On the other hand, values of k_{smec} in the range of 0.5–5 of L22–L113 may imply that the direction of fracture propagation, which promoted hydrothermal alteration to produce smectite, differed from core to core. In addition, these values might reflect the igneous lamination of the protolith (e.g., Best, 2002). However, no data on the anisotropy of smectite distribution and preferred orientation were available to validate the optimized parameters in Table 12; thus, we do not discuss them further.

3.2. Dependence of Bulk Conductivity on Petrophysical Properties in Smectite-Bearing Rocks

Here, we show the simulation results under the wide parameter ranges listed in Table 11. In all conditions, simulations were performed for 10 different random configurations to obtain the conductivities in the *X*, Y, and Z axis directions; thus, we have 30 pieces of simulated conductivity data for each condition. The contribution of the EDL on quartz to the bulk conductivity was not discussed here because it was minimal (<0.06 S m^{-1}) across all petrophysical conditions considered.

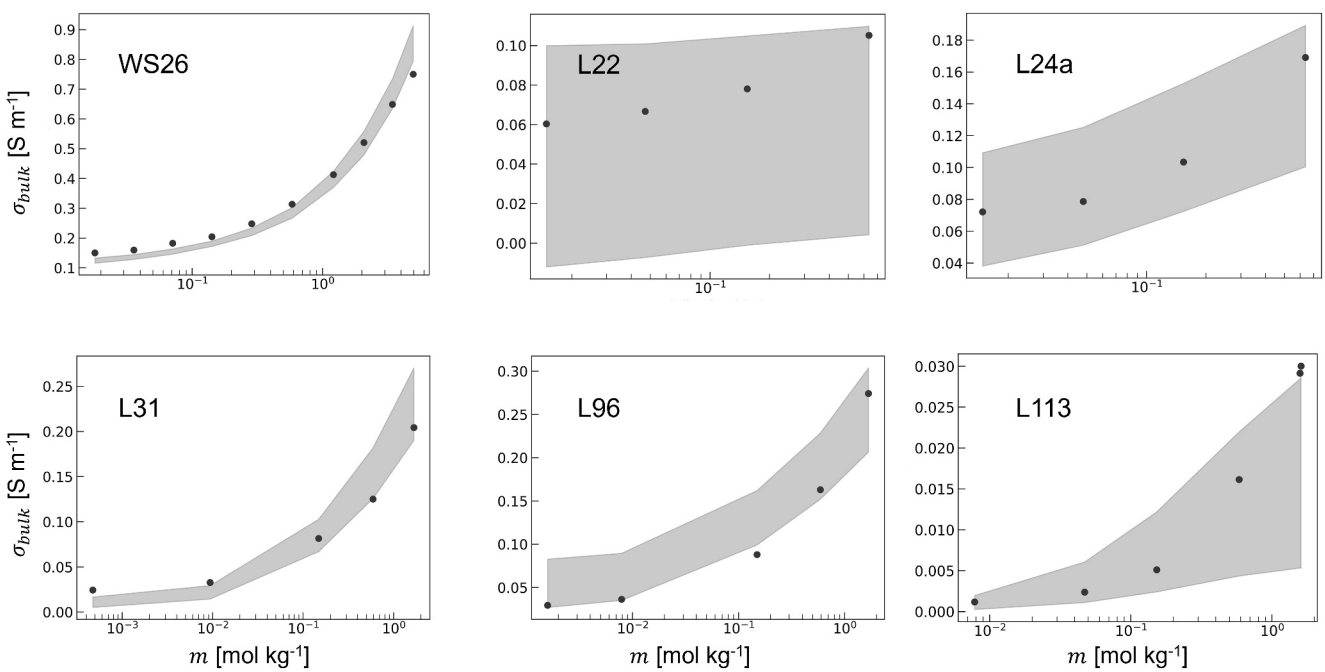

Figure 11. Comparison of the experimental data (dots) and simulator output (gray area). The best-fit parameter values are listed in Table 12. The gray areas indicate the average ± standard deviation estimated from 100 realizations of the simulations. The vertical and horizontal axes show the bulk conductivity in the *X*-axis (in S m^{-1}) and molality (mol kg^{-1}), respectively.

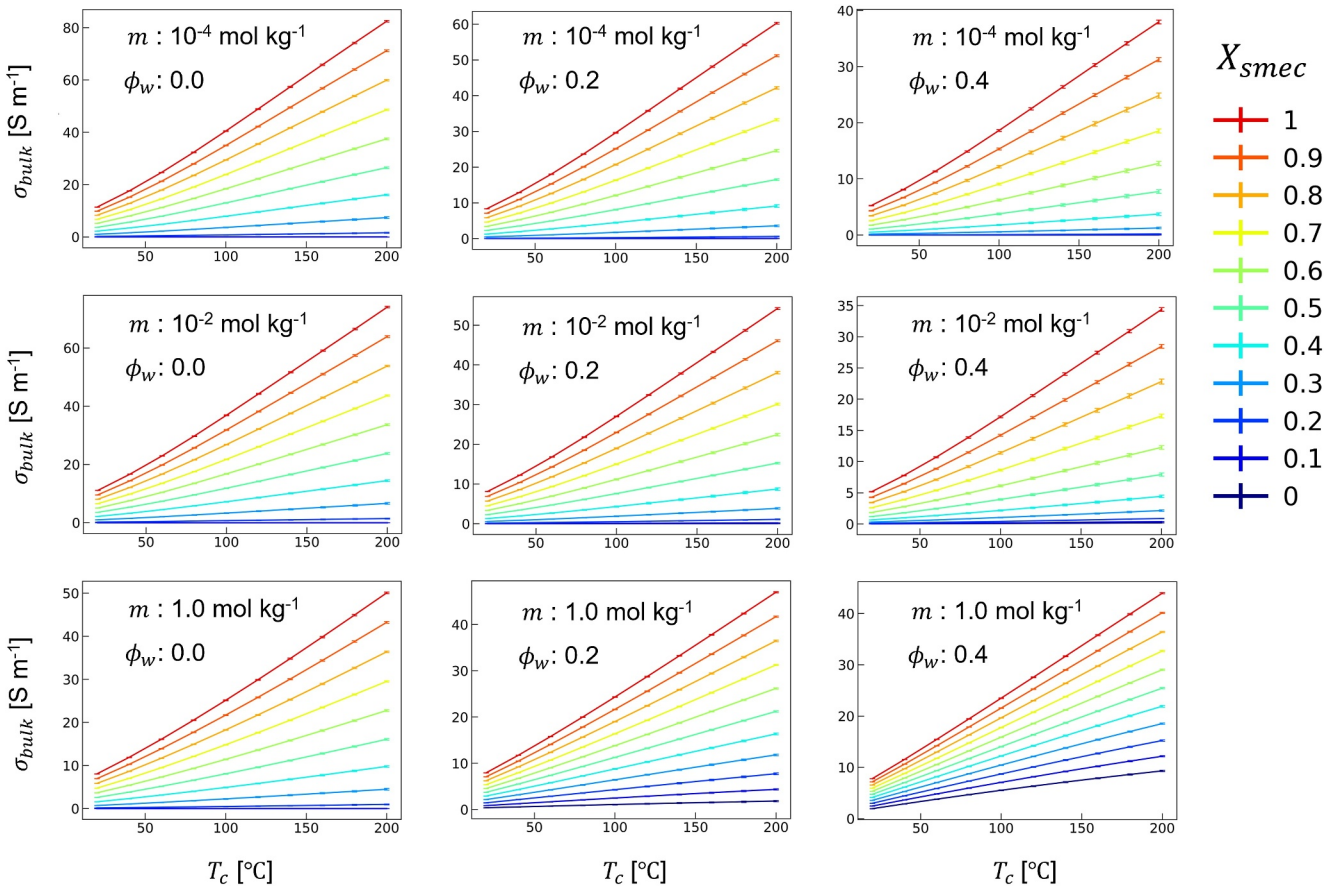

Figure 12. Temperature dependence of bulk conductivity at different salinity (m), porosity (ϕ_w: volume fraction of macropore), and smectite fraction (X_{smec}). Error bars indicate standard deviations estimated using 30 pieces of simulated conductivity data for each condition based on the random assignment of components.

3.2.1. Temperature Dependence

For any salinity, porosity, and smectite content, the temperature dependence of the bulk conductivity was linear (Figure 12). This linear slope arises from the linear nature of the temperature dependence of the conductivity for each component. On the other hand, above 200°C, these linear dependences might disappear due to the nonlinear temperature dependence of the conductivity of NaCl solution (e.g., Watanabe et al., 2021) and the electrochemical properties of smectite (Equations 23–43). The greater slope of the bulk conductivity versus temperature with increasing smectite content is attributed to the greater temperature dependence of smectite than that of the NaCl solution (Figure 7). While the temperature dependence of the conductivity of the EDL on quartz is approximately three times larger than that of smectite or NaCl solution in the normalized plot (Figure 7), its contribution is negligible compared to smectite because of the small conductivity (10^{-12} S m^{-1}) of quartz.

3.2.2. Salinity Dependence

Regions of negative slopes of bulk conductivity with increasing salinity appeared when the rock contained sufficient smectite (Figure 13). This negative slope is because, at molalities below 1 mol kg^{-1}, Na^+ ions concentrate in the Stern layer, where mobility decreases monotonically with increasing salinity (Figure 14). Conversely, at molalities exceeding 1 mol kg^{-1}, the conductivity of the interlayer begins to increase because of the increased proportion of Na^+ in the diffuse layer, where the ion mobility is greater than that of the Stern layer. The negative slopes of the interlayer conductivity have been confirmed by MD simulations (Greathouse et al., 2016) and EMT analysis (Revil et al., 1998, Figure 5b herein). However, to our knowledge, experimental studies have not supported this, potentially owing to the following three factors.

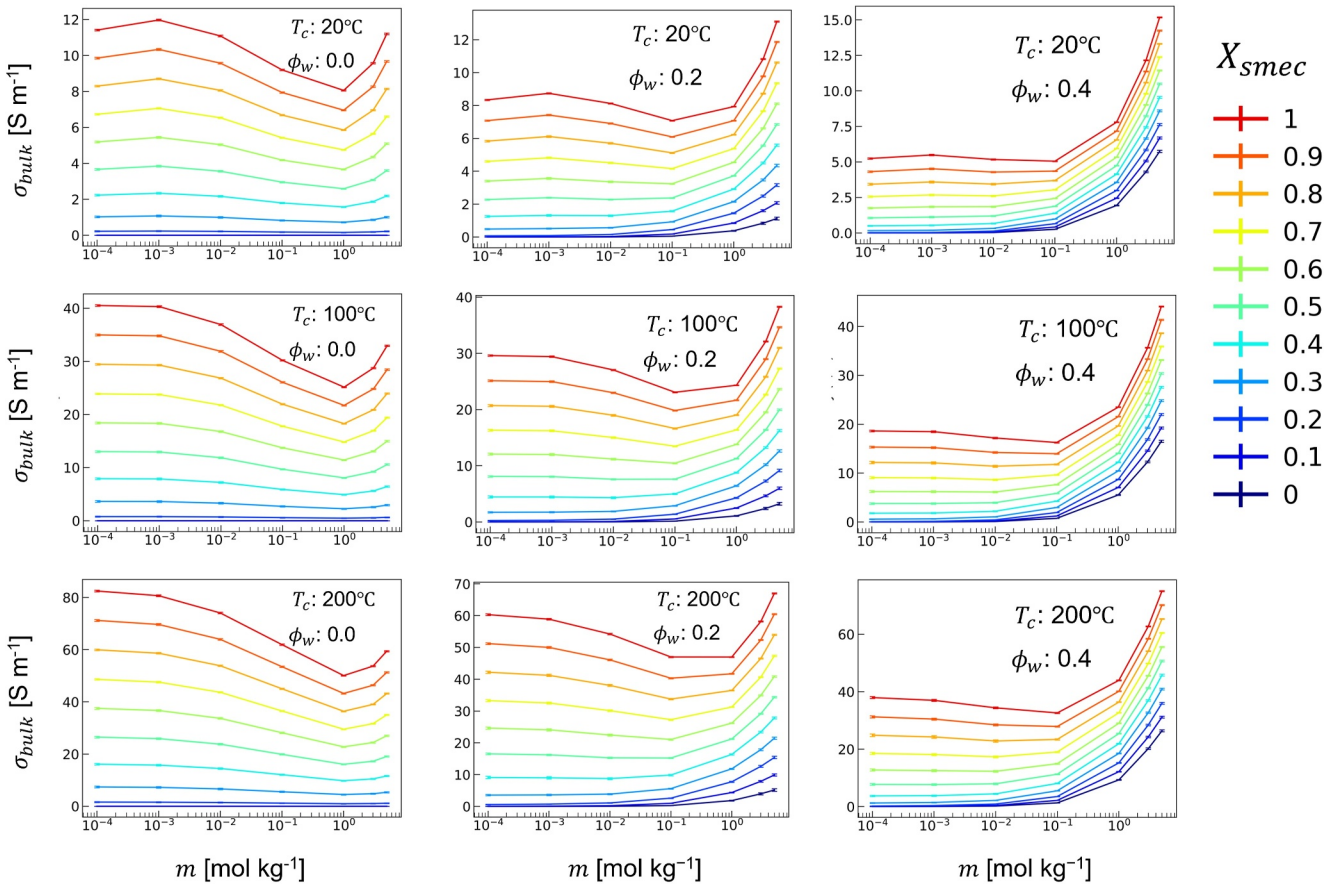

Figure 13. Molality dependence of bulk conductivity at different temperatures (T_c), porosities (ϕ_w: volume fraction of macropore), and smectite fractions (X_{smec}). Error bars indicate standard deviations estimated using 30 pieces of simulated conductivity data for each condition based on the random assignment of components.

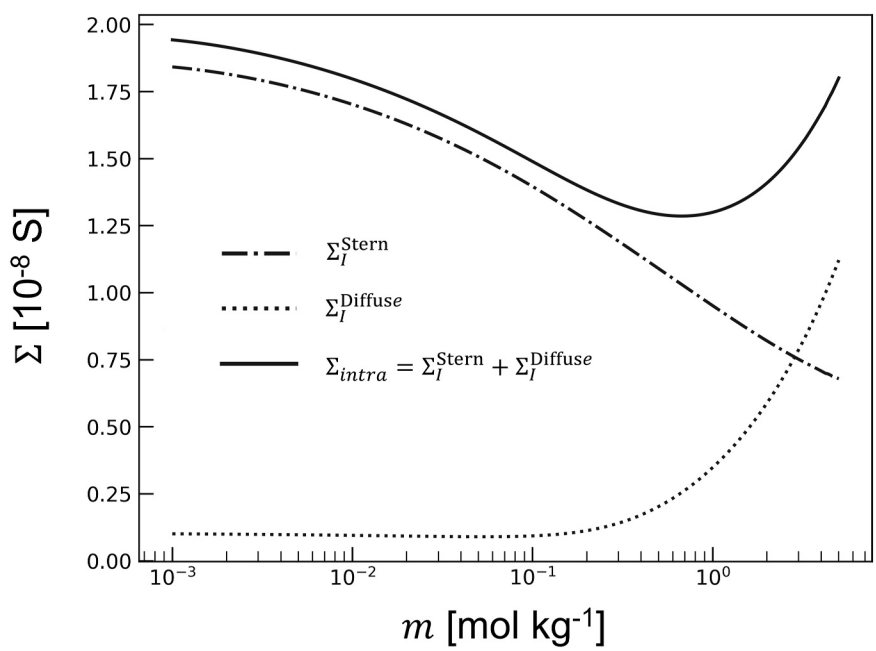

Figure 14. Molality dependence of the conductance of an interlayer ($2r$ = 2 nm; T_c = 20°C; P = 5 MPa).

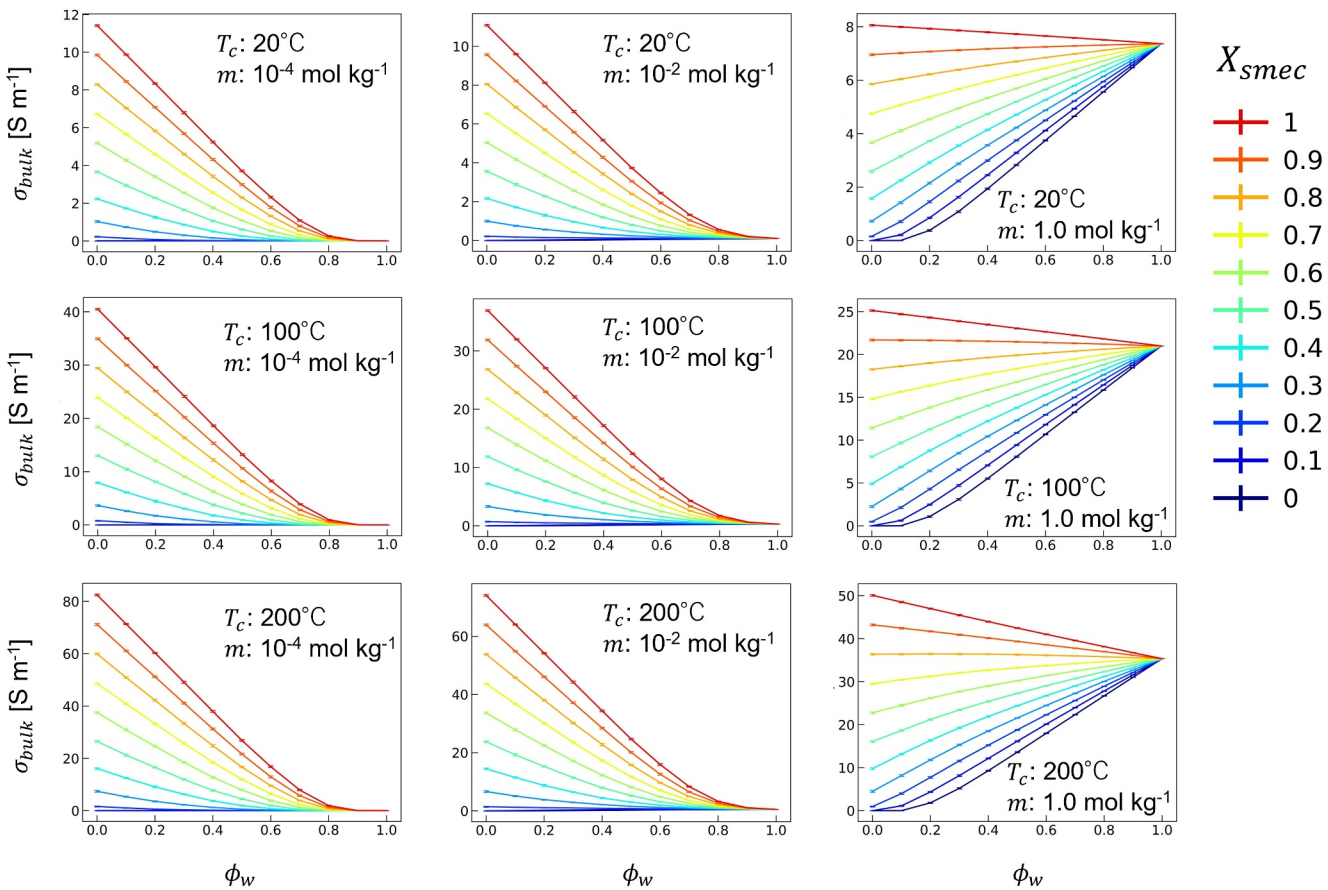

Figure 15. Porosity dependence of bulk conductivity at different temperatures (T_c), molalities (m), and smectite fractions (X_{smec}). Error bars indicate standard deviations estimated using 30 pieces of simulated conductivity data for each condition based on the random assignment of components.

1. X_{smec} of cores for which the bulk conductivity has been measured in previous studies is generally less than 0.5 (e.g., Lévy et al., 2018). The pore water conduction dominates the bulk conductivity at low smectite content, which always increases with salinity (Figure 1). In addition, the degree of clay alteration is positively correlated with porosity (Lévy et al., 2018); therefore, core samples with low porosity and high smectite content, where negative slopes appear, may rarely be found.
2. In actual core samples, interlayer thickness decreases with increasing salinity (e.g., Svensson & Hansen, 2013). Thus, the current through the macropores is expected to increase with increasing salinity.
3. Conductivity measurements of samples with high clay mineral content require a significant effort. For instance, the viscous properties and swelling pressure make it challenging to place or remove them from a sample holder (Takakura, 2009). Additionally, achieving chemical equilibrium can take several months (Waxman & Smits, 1968).

3.2.3. Porosity Dependence

When the salinity is low ($\leq 10^{-2}$ mol kg^{-1}) and smectite is present in a rock, the slope of the bulk conductivity to the porosity is negative (Figure 15) (note that in this section, we use porosity to mean the volume fraction of macropore: ϕ_w). If the salinity is 10^{-2} mol kg^{-1} or less, the conductivity of the interlayer exceeds that of the macropore by over 100 times. Thus, the current path is concentrated in the smectite. Therefore, as porosity increases, the total current decreases as the volume fraction of smectite in the entire rock ($= [1 - \phi_w]X_{smec}$) decreases. Conversely, for a salinity of 1 mol kg^{-1}, the predominant current pathway shifts from smectite to the macropore, and curves with a very high smectite content ($X_{smec} \geq 0.9$) alone have negative slopes, whereas others show a typical feature of Archie's law (Archie, 1942). To our knowledge, no previous experimental studies using real samples have reported such a negative slope in smectite-bearing rocks. It would be difficult to conduct

experiments on actual rocks in which the macro-porosity alone is changed without affecting other petrophysical properties. The ability to replicate experiments under such difficult conditions is an advantage of numerical simulation. In two-component systems with Cu_2O and NaCl solutions, similar behavior has been reported for NaCl concentrations below 10^{-2} M (Glover et al., 2000).

3.3. Comparison With Previous Models

Among the seven equations proposed in previous studies, our simulator best fitted Clavier et al.'s (1984) equation, which showed the highest R^2 with the lowest Akaike information criterion (AIC) (Table 13). However, the assumption in this equation that the ion mobility in the EDL increases with increasing salt concentration needs to be corrected, considering the discussion in Section 3.2.2. Moreover, although this equation has the smallest AIC among those proposed in previous studies, it has eight free parameters. Therefore, instead of further complexing it, we modified the equation of Qi and Wu (2022) derived from the EMT, which is an easy-to-use explicit function with fewer free parameters. By introducing additional parameters for the dependence of the effective EDL conductivity (σ_r) on fluid conductivity, the modified equation of Qi and Wu (2022) yielded an AIC smaller than that of Clavier et al. (1984) with an equivalent R^2 (Table 13). It may also be used to interpret experimental data, as the original equation of Qi and Wu (2022) is capable of such purposes.

Archie's equation (Archie, 1942) cannot be applied to interpret the conductivity of smectite-bearing rocks because it is valid only for binary systems comprising an insulator and a conductor (e.g., Bussian, 1983). Furthermore, while Archie's equation did not reproduce the simulation results well, replacing ϕ_w with ϕ ($= \phi_w + \phi_{smec}$, where $\phi_{smec} = 2(1-\phi_w)rX_{smec}/[2r + d_{TOT}]$) resulted in better R^2 and AIC (Table 13). This result implies that we should know which region is included in the "porosity" used to interpret the conductivity of shaly sands with Archie's type formation factor.

3.4. Percolation Thresholds of Smectite-Bearing Rock

To investigate the percolation threshold, we performed simulations by varying ϕ_w and X_{smec} in 0.01 increments in the ranges of $0 \le \phi_w \le 0.2$ and $0 \le X_{smec} \le 0.2$ with the conditions listed in Tables 9 and 11 (temperature, pore pressure, and molality are fixed at 20°C, 5 MPa, and 0.1 mol kg^{-1}, respectively). We observed a significant change in bulk conductivity on a logarithmic scale when the sum of ϕ_w and X_{smec} (approximately equal to ϕ_{smec} at low ϕ_w) reached 0.1 (Figure 16). This value is close to the percolation threshold of 0.0976 reported by Kurzawski and Malarz (2012) for a randomly assigned binary mixture of an insulator and a conductor using the criteria of a 26-site coordination number (i.e., Rubik's neighborhood named in that study). By employing *NeworkX* (a software to analyze graphs comprising nodes and edges) (Jung, 2022) with Rubik's neighborhood criteria, we further confirmed that when the sum of ϕ_w and ϕ_{smec} reaches 0.1, smectite and macropore paths begin to connect from one end of the specimen to the other (Figure 17). Below the percolation threshold, independent clusters with a small localized current flow were observed (Figure 18a). At the percolation threshold, current pathways emerged along conduits comprising NaCl solution and smectite (Figure 18b). Above the percolation threshold, almost all NaCl solutions and smectite contributed to the current paths (Figure 18c).

4. Conclusions

To accurately compute the direct-current conductivity of smectite-bearing rocks across varied temperatures, salinities, and porosities, we developed a simulator capable of reproducing the conduction phenomenon in rocks composed of aqueous NaCl solution, quartz, and smectite. By considering the geometric parameters of the rock, the simulator reproduced the experimental data of core samples in previous studies. Simulations with randomly assigned components revealed that when rock specimens contain abundant smectite, the bulk conductivity partially decreases with increasing NaCl solution's salinity or volume fraction. To our knowledge, this study is the first to validate the presence of these negative slopes. We confirmed that such characteristics can also be reproduced using the equations of Clavier et al. (1984) or the partially modified version of Qi and Wu (2022). In addition, we found that current paths between the ends of the specimen start to form when the sum of the volume fraction of macropores and smectite reaches 0.1. An effective application of our simulator is the interpretation of shallow subsurface structures, particularly those containing smectite-bearing rocks. This includes evaluating

Table 13
Equations Tested to Reproduce the Results of Numerical Experiments With Optimized Parameters, Coefficient of Determination (R^2), and Akaike's Information Criterion (AIC)

Previous works	Equations	Optimized parameters	R^2	AIC
Archie (1942)	$\sigma_{\mathrm{bulk}} = {\phi_w}^m \sigma_w$	$m = 1.0$	−0.09	3.4×10^4
	$\sigma_{\mathrm{bulk}} = \phi^m \sigma_w$	$m = 1.5$	0.27	3.3×10^4
Wyllie and Southwick (1954) [a, b]	$\sigma_{\mathrm{bulk}} = \frac{1}{F}\sigma_w + \frac{\sigma_r+\sigma_w}{x\sigma_r+y\sigma_w} + z\sigma_r$, with $\sigma_r = c'\phi_{\mathrm{smec}}\{1+\alpha(T_c-20)\}$	$F = 6.3$, $x = 1.0 \times 10^{-11}$, $y = 1.7 \times 10^{-3}$, $z = 5.5 \times 10^2$, $\alpha = 4.2 \times 10^{-2}$, $c' = 7.6 \times 10^{-3}$	0.76	2.4×10^4
Waxman and Thomas (1974)	$\sigma_{\mathrm{bulk}} = \phi^m(\sigma_w + BQ_v)$, with $B = \exp(-E/T)(1 - a\exp(-\sigma_w/\gamma))$, and $Q_v = c'\phi_{smec}$	$m = 1.9$, $a = 0.14$, $\gamma = 2.1 \times 10^{-5}$, $E = 1.5 \times 10^3$, $c' = 2.8 \times 10^3$	0.70	2.6×10^4
Bussian (1983) [a, b]	$\sigma_{\mathrm{bulk}} = \sigma_w\phi^m\left(\frac{1-\sigma_w/\sigma_r}{1-\sigma_{bulk}/\sigma_r}\right)^m$, with $\sigma_r = c'\phi_{\mathrm{smec}}\{1+\alpha(T_c-20)\}$	$m = 1.7$, $\alpha = 1.25$, $c' = 9.3 \times 10^{-2}$	0.30	3.3×10^4
Clavier et al. (1984)	$\sigma_{\mathrm{bulk}} = \phi^m[(1 - v_Q Q_v)\sigma_w + \beta Q_v]$, with $v_Q = \frac{\alpha(22+b)}{T+b}$, $\beta = \lambda\left\{1 - a\exp\left(-\frac{\sigma_w}{\gamma}\right)\right\}\frac{T+22}{c+22}$, and $Q_v = c'\phi_{\mathrm{smec}}$	$m = 1.4$, $a = 0.24$, $b = 5.0 \times 10^5$, $c = 5.5$, $\alpha = 0.45$, $\gamma = 3.5 \times 10^{-6}$, $\lambda = 5.0$, $c' = 3.4$	0.93	2.1×10^4
Sen and Goode (1992)	$\sigma_{\mathrm{bulk}} = \phi^m\left(\sigma_w + \frac{Dm\mu_T Q_v}{1+\frac{C\mu_T}{\sigma_w}}\right) + E\phi^m\mu_T Q_v$, with $\mu_T = 1 + \alpha(T_c - 22)$, and $Q_v = c'\phi_{\mathrm{smec}}$	$m = 1.9$, $C = 7.4 \times 10^{-2}$, $D = 9.9 \times 10^{-13}$, $E = 3.1$, $\alpha = 0.20$, $c' = 1.1$	0.70	2.6×10^4
Qi and Wu (2022) [a, b]	$\sigma_{\mathrm{bulk}} = \frac{\sigma_w}{F} + \frac{(2\xi+1)\sigma_r\sigma_w + 2(1-\xi){\sigma_r}^2}{(2+\xi)\sigma_r + (1-\xi)\sigma_w}$, with $\sigma_r = c'\phi_{\mathrm{smec}}\{1+\alpha(T_c-20)\}$	$\zeta = 6.2 \times 10^{-8}$, $F = 6.2$, $\alpha = 0.91$, $c' = 0.47$	0.75	2.4×10^4
Modified Qi and Wu (2022)	$\sigma_{\mathrm{bulk}} = \phi^m\sigma_w + \frac{(2\xi+1)\sigma_r\sigma_w + 2(1-\xi){\sigma_r}^2}{(2+\xi)\sigma_r + (1-\xi)\sigma_w}$, with $\sigma_r = c'\phi_{\mathrm{smec}}\{1+\alpha(T_c-20)\}(a{\sigma_w}^2 + b\sigma_w + c)$	$\zeta = 1.60 \times 10^{-10}$, $m = 1.52$, $\alpha = 6.7 \times 10^{-2}$, $a = 0.63$, $b = -1.1 \times 10^2$, $c = 4.5 \times 10^3$, $c' = 1.3 \times 10^{-3}$	0.93	1.9×10^4

Note. Independent variables are σ_{bulk} (bulk conductivity; in S m^{-1}), σ_w (in S m^{-1}), T_c (in °C), T (in K), ϕ_w (volume fraction of macropore), ϕ_{smec} (volume fraction of smectite; $\phi_{\mathrm{smec}} = 2r(1-\phi_w)X_{\mathrm{smec}}/[2r + d_{\mathrm{TOT}}]$), and ϕ (effective porosity, including microporosity of the interlayer; i.e., $\phi = \phi_w + \phi_{\mathrm{smec}}$). The others are free parameters (i.e., parameters to be fitted). Symbols are derived from previous studies. The curve-fitting was performed using the simulated data with $\phi_w \leq 0.5$. [a]Although those studies did not consider the salinity dependence of EDL conductivity, they reproduced the salinity dependence of bulk conductivity of shaly sands. Therefore, we did not incorporate the salinity dependence in our study. [b]As the temperature dependence of the EDL conductivity was not addressed in those studies, our study incorporated the corresponding parameters into the equation.

geothermal resources and identifying potential landslide layers. However, achieving accurate interpretation depends on appropriately constrained petrophysical properties, which can be attained through drilling or cross-checking with other methods.

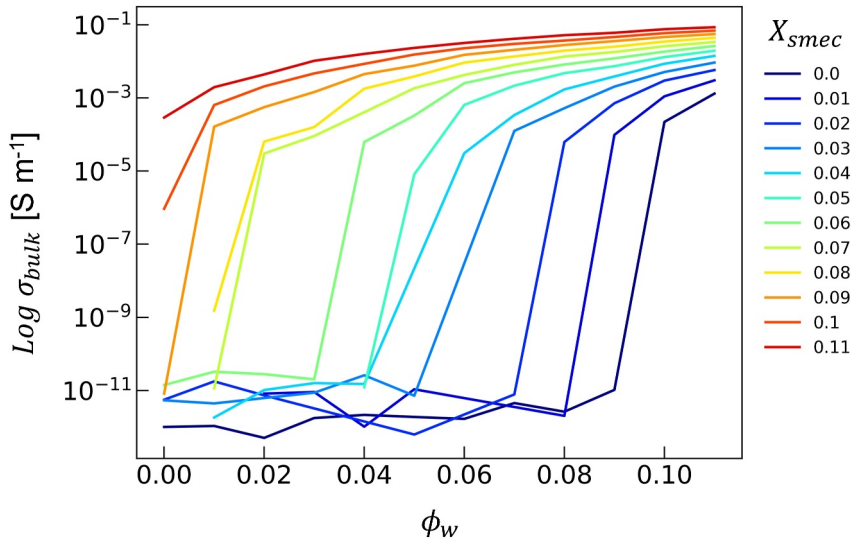

Figure 16. Bulk conductivity of the smectite-bearing rock in $0 \leq \phi_w \leq 0.2$ and $0 \leq X_{smec} \leq 0.2$. The lines indicate the average of 30 pieces of simulated conductivity data.

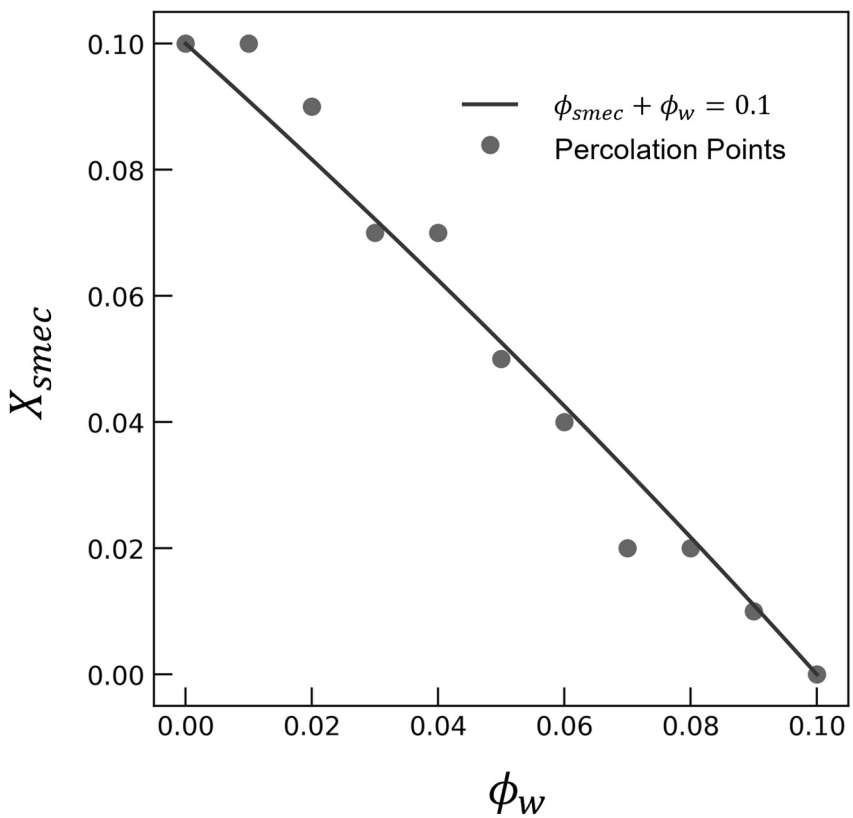

Figure 17. Plot of percolation points from network analysis and curve of $\phi_w + \phi_{smec} = 0.1$ ($\phi_{smec} = (1 - \phi_w)X_{smec}$). The percolation points indicate the conditions under which at least one path was formed from end to end out of 10 random arrangements.

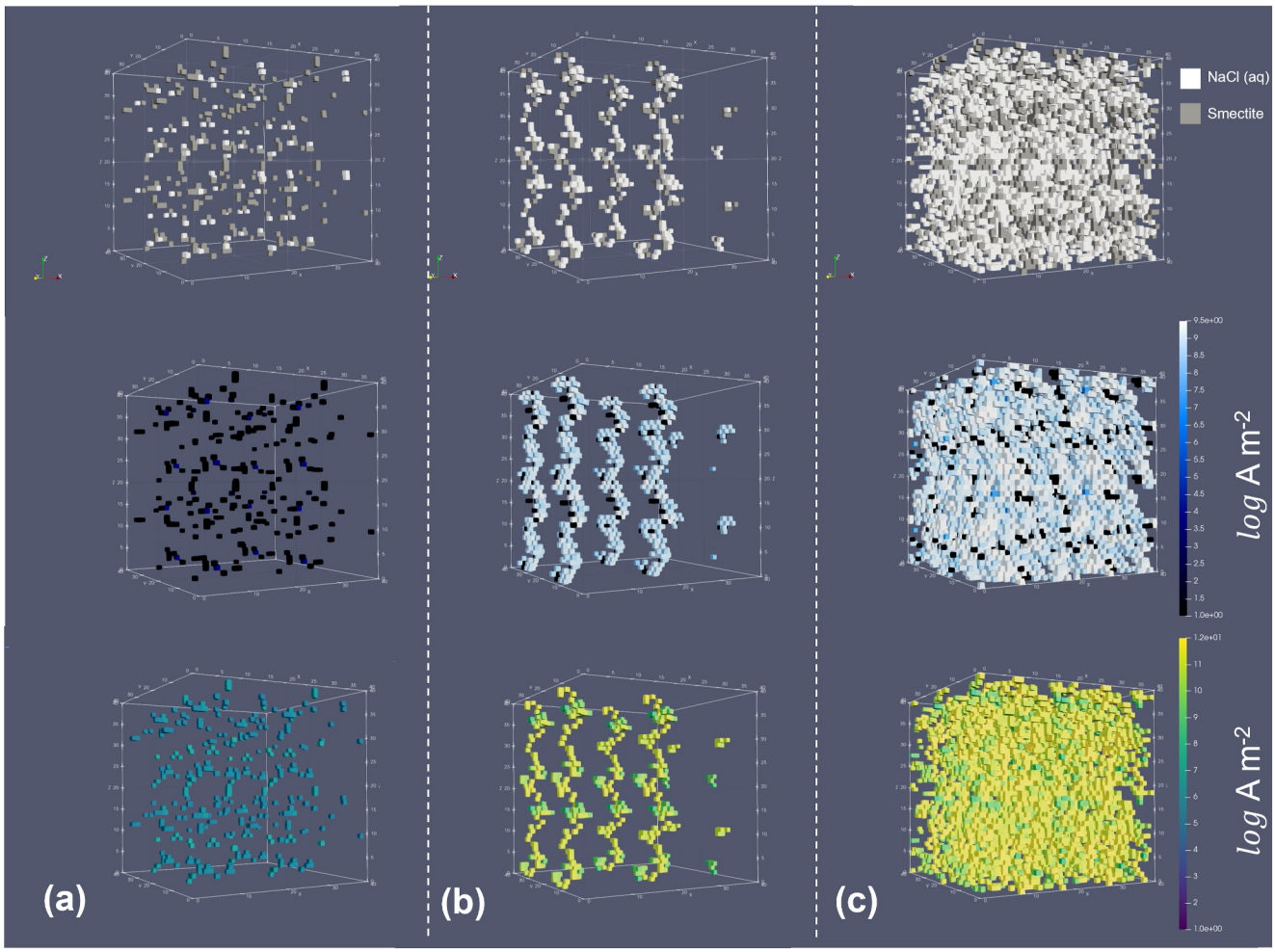

Figure 18. Three-dimensional views of current paths near the percolation threshold. The top panel shows the arrangement of the NaCl solution and smectite, the middle panel shows the magnitude of the surface current density, and the bottom panel shows the magnitude of the volume current density. (a) $X_{smec} = 0.05$ and $\phi_w = 0.02$. (b) $X_{smec} = 0.05$ and $\phi_w = 0.05$. (c) $X_{smec} = 0.05$ and $\phi_w = 0.08$. Considering the periodic boundary conditions, we plotted a region two times larger than the computational domain. A voltage of 20 V was equally and simultaneously applied to all three axes (Table 9).

Data Availability Statement

Experimental data from Lévy et al. (2018), Rasmusson et al. (1997), Sen and Goode (1992), Sonnefeld et al. (2001), Watillon and de Backer (1970), Waxman and Smits (1968), and Yamamoto and Namikawa (1994) were used in this study. As noted in the caption of Figure 3, some of the data from Sonnefeld et al. (2001) and Watillon and de Backer (1970) were compiled from Leroy et al. (2013) and Revil et al. (1998), respectively. In addition, analytical results from Bourg and Sposito (2011), Clavier et al. (1984), Revil et al. (1998), Sen and Goode (1992), Tournassat et al. (2009), Waxman and Thomas (1974), Zhang et al. (2011), and Zhang et al. (2014) were used. If numerical data were available in the literature, they were referenced; otherwise, the data in the graphs were numerically converted using WebPlotDigitizer (Rohatgi, 2015). The software developed in this study is licensed under GPL-3.0 and published on the open-access repository (Aoyama, 2024). Those codes were written in Python 3.9.15 and implemented by *NumPy* (Harris et al., 2020), *SciPy* (Virtanen et al., 2020), and *iapws* (Romera, 2021). All graphs in this manuscript were created using *Matplotlib* (Caswell et al., 2022; Hunter, 2007) and *ParaView* (Ahrens et al., 2005). The network analysis and non-linear regression were conducted using *NetworkX* (Jung, 2022) and *lmfit* (Newville et al., 2023), respectively.

Acknowledgments
This work was supported by JST SPRING, Grant No. JPMJSP2119. The authors would like to thank the National Institute of Standards and Technology and Edward J. Garboczi for publishing the FEM's computing codes. We would also like to acknowledge the fruitful discussions on this research with Léa Lévy, Toshiaki Hokari, Tomohiro Inoue, Tatsuto Oishi, Juo-hua Pan, and Ayuta Tsuge.

References

Ahrens, J., Geveci, B., & Law, C. (2005). ParaView: An end-User Tool for large data Visualization [Software]. *Los Alamos National Laboratory*, 717–731. https://doi.org/10.1016/b978-012387582-2/50038-1

Alizadeh, A., & Wang, M. (2020). Temperature effects on electrical double layer at solid-aqueous solution interface. *Electrophoresis*, *41*(12), 1067–1072. https://doi.org/10.1002/elps.201900354

Aoyama, K. (2024). Effective electrical conductivity simulator for rocks [Software]. https://doi.org/10.5281/zenodo.12871737

Archie, G. E. (1942). The electrical resistivity log as an aid in determining some reservoir characteristics. *Transactions of the American Institute of Mining and Metallurgical Engineers*, *146*(01), 54–61. https://doi.org/10.2118/942054-G

Árnason, K., Karlsdóttir, R., Eysteinsson, H., Flóvenz, Ó. G., & Gudlaugsson, S. T. (2000). The resistivity structure of high-temperature geothermal systems in Iceland. In *Proceedings World geothermal Congress 2000* (pp. 923–928).

Bannard, J. E. (1975). Effect of density on the electrical conductance of aqueous sodium chloride solutions. *Journal of Applied Electrochemistry*, *5*(1), 43–53. https://doi.org/10.1007/BF00625958

Best, G. M. (2002). *Igneous and Metamorphic Petrology* (2nd ed.). Blackwell Science.

Bourg, I. C., & Sposito, G. (2011). Molecular dynamics simulations of the electrical double layer on smectite surfaces contacting concentrated mixed electrolyte (NaCl-CaCl2) solutions [Dataset]. *Journal of Colloid and Interface Science*, *360*(2), 701–715. https://doi.org/10.1016/j.jcis.2011.04.063

Bowles, F. A. (1968). Microstructure of sediments – Investigation with ultrathin sections. *Science*, *159*(3820), 1236–1237. https://doi.org/10.1126/science.159.3820.1236

Bussian, A. E. (1983). Electrical conductance in a porous-medium. *Geophysics*, *48*(9), 1258–1268. https://doi.org/10.1190/1.1441549

Castro, J., Asta, M. P., Galve, J. P., & Azañón, J. M. (2020). Formation of clay-rich layers at the slip surface of slope instabilities: The role of groundwater. *Water*, *12*(9), 2639. https://doi.org/10.3390/w12092639

Caswell, T. A., Lee, A., Droettboom, M., de Andrade, E. S., Hoffmann, T., Klymak, J., et al. (2022). matplotlib/matplotlib: Rel: v3.6.2 (v3.6.2) [Software]. *Zenodo*. https://doi.org/10.5281/zenodo.7275322

Clavier, C., Coates, G., & Dumanoir, J. (1984). Theoretical and experimental bases for the dual water model for interpretation of shaly sands [Dataset]. *Society of Petroleum Engineers Journal*, *24*(2), 153–168. https://doi.org/10.2118/6859-PA

Cohen-Adad, R., & Lorimer, J. W. (1991). *Alkali metal and ammonium chlorides in water and heavy water (binary systems), 1–209, IUPAC Solubility Data Series*. Pergamon.

Driesner, T. (2007). The system H2O-NaCl.: Part II:: Correlations for molar volume, enthalpy, and isobaric heat capacity from 0 to 1000 °C, 1 to 5000 bar, and 0 to 1 XNaCl. *Geochimica et Cosmochimica Acta*, *71*(20), 4902–4919. https://doi.org/10.1016/j.gca.2007.05.026

Fu, J., Thomas, H. R., & Li, C. (2021). Tortuosity of porous media: Image analysis and physical simulation. *Earth-Science Reviews*, *212*, 103439. https://doi.org/10.1016/j.earscirev.2020.103439

Garboczi, E. J. (1998). *Finite element and finite difference programs for computing the linear electric and elastic properties of digital images of random materials* (Vols. 1–14). National Institute of Standards and Technology.

Glover, P. W. J., Hole, M. J., & Pous, J. (2000). A modified Archie's law for two conducting phases. *Earth and Planetary Science Letters*, *180*(3–4), 369–383. https://doi.org/10.1016/S0012-821X(00)00168-0

Gonçalvès, J., Rousseau-Gueutin, P., & Revil, A. (2007). Introducing interacting diffuse layers in TLM calculations: A reappraisal of the influence of the pore size on the swelling pressure and the osmotic efficiency of compacted bentonites. *Journal of Colloid and Interface Science*, *316*(1), 92–99. https://doi.org/10.1016/j.jcis.2007.07.023

Greathouse, J. A., Cygan, R. T., Fredrich, J. T., & Jerauld, G. R. (2016). Molecular dynamics simulation of diffusion and electrical conductivity in montmorillonite interlayers. *Journal of Physical Chemistry C*, *120*(3), 1640–1649. https://doi.org/10.1021/acs.jpcc.5b10851

Harris, C. R., Millman, K. J., van der Walt, S. J., Gommers, R., Virtanen, P., Cournapeau, D., et al. (2020). Array programming with NumPy [software]. *Nature*, *585*(7825), 357–362. https://doi.org/10.1038/s41586-020-2649-2

Hunter, J. D. (2007). Matplotlib: A 2D graphics environment [Software]. *Computing in Science & Engineering*, *9*(3), 90–95. https://doi.org/10.1109/MCSE.2007.55

IAPWS. (2008). Release on the IAPWS formulation 2008 for the viscosity of ordinary water substance, 1-9, 2008 International association for the properties of water and Steam.

Jung, S. (2022). Networkx graph generation algorithm sample binary graphs [Software]. *Zenodo*. https://doi.org/10.5281/zenodo.6547767

Kaufhold, S., Grissemann, C., Dohrmann, R., Klinkenberg, M., & Decher, A. (2014). Comparison of three small-scale devices for the investigation of the electrical conductivity/resistivity of swelling and other clays. *Clays and Clay Minerals*, *62*(1–2), 1–12. https://doi.org/10.1346/CCMN.2014.0620101

Kawamura, K. (2010). Burial consolidation process of deep-sea sediments: An example of core sediments collected from the Labrador sea in the northwest Atlantic. *Soils and Foundations*, *50*(5), 623–632. https://doi.org/10.3208/sandf.50.623

Klyukin, Y. I., Lowell, R. P., & Bodnar, R. J. (2017). A revised empirical model to calculate the dynamic viscosity of H2O-NaCl fluids at elevated temperatures and pressures (≤1000 °C, ≤500 MPa, 0-100 wt % NaCl). *Fluid Phase Equilibria*, *433*, 193–205. https://doi.org/10.1016/j.fluid.2016.11.002

Kurzawski, L., & Malarz, K. (2012). Simple cubic random-site percolation thresholds for complex neighborhoods. *Reports on Mathematical Physics*, *70*(2), 163–169. https://doi.org/10.1016/S0034-4877(12)60036-6

Leroy, P., Devau, N., Revil, A., & Bizi, M. (2013). Influence of surface conductivity on the apparent zeta potential of amorphous silica nanoparticles [Dataset]. *Journal of Colloid and Interface Science*, *410*, 81–93. https://doi.org/10.1016/j.jcis.2013.08.012

Leroy, P., Maineult, A., Li, S., & Vinogradov, J. (2022). The zeta potential of quartz. Surface complexation modelling to elucidate high salinity measurements. *Colloids and Surfaces A: Physicochemical and Engineering Aspects*, *650*, 129507. https://doi.org/10.1016/j.colsurfa.2022.129507

Leroy, P., & Revil, A. (2004). A triple-layer model of the surface electrochemical properties of clay minerals. *Journal of Colloid and Interface Science*, *270*(2), 371–380. https://doi.org/10.1016/j.jcis.2003.08.007

Leroy, P., & Revil, A. (2009). A mechanistic model for the spectral induced polarization of clay materials. *Journal of Geophysical Research: Solid Earth*, *114*(B10). https://doi.org/10.1029/2008JB006114

Leroy, P., Tournassat, C., Bernard, O., Devau, N., & Azaroual, M. (2015). The electrophoretic mobility of montmorillonite. Zeta potential and surface conductivity effects. *Journal of Colloid and Interface Science*, *451*, 21–39. https://doi.org/10.1016/j.jcis.2015.03.047

Lévy, L., Gibert, B., Sigmundsson, F., Flóvenz, Ó. G., Hersir, G. P., Briole, P., & Pezard, P. A. (2018). The role of smectites in the electrical conductivity of active hydrothermal systems: Electrical properties of core samples from Krafla volcano, Iceland [Dataset]. *Geophysical Journal International*, *215*(3), 1558–1582. https://doi.org/10.1093/gji/ggy342

Mao, S., Hu, J., Zhang, Y., & Lü, M. (2015). A predictive model for the PVTx properties of CO_2–H_2O–NaCl fluid mixture up to high temperature and high pressure. *Applied Geochemistry*, *54*, 54–64. https://doi.org/10.1016/j.apgeochem.2015.01.003

Masuda, T., Michibayashi, K., & Ohta, H. (1995). Shape preferred orientation of rigid particles in a viscous matrix – Reevaluation to determine kinematic parameters of ductile deformation. *Journal of Structural Geology*, *17*(1), 115–129. https://doi.org/10.1016/0191-8141(94)E0026-U

Monnin, C. (1990). The Influence of pressure on the activity coefficients of the solutes and on the solubility of minerals in the system Na-Ca-Cl-SO4-H2O to 200°C and 1 kbar, and to high NaCl concentration. *Geochimica et Cosmochimica Acta*, *54*(12), 3265–3282. https://doi.org/10.1016/0016-7037(90)90284-R

Newville, M., Otten, R., Nelson, A., Stensitzki, T., Ingargiola, A., Allen, D., et al. (2023). lmfit/lmfit-py: 1.2.1 [Software]. https://doi.org/10.5281/zenodo.7887568

Pitzer, K. S. (1973). Thermodynamics of electrolytes .1. Theoretical basis and general equations. *Journal of Physical Chemistry*, *77*(2), 268–277. https://doi.org/10.1021/j100621a026

Qi, Y., & Wu, Y. (2022). Electrical conductivity of clayey rocks and soils: A non-linear model. *Geophysical Research Letters*, *49*(10). https://doi.org/10.1029/2021GL097408

Rasmusson, M., Rowlands, W., O'Brien, R. W., & Hunter, R. (1997). The dynamic mobility and dielectric response of sodium bentonite [Dataset]. *Journal of Colloid and Interface Science*, *189*(1), 92–100. https://doi.org/10.1006/jcis.1997.4793

Raspo, I., & Neau, E. (2020). An empirical correlation for the relative permittivity of liquids in a wide temperature range: Application to the modeling of electrolyte systems with a GE/EoS approach. *Fluid Phase Equilibria*, *506*, 112371. https://doi.org/10.1016/j.fluid.2019.112371

Revil, A., CathlesIII, L. M., Losh, S., & Nunn, J. A. (1998). Electrical conductivity in shaly sands with geophysical applications [Dataset]. *Journal of Geophysical Research: Solid Earth*, *103*(B10), 23925–23936. https://doi.org/10.1029/98JB02125

Revil, A., & Glover, P. W. J. (1997). Theory of ionic-surface electrical conduction in porous media. *Physical Review B*, *55*(3), 1757–1773. https://doi.org/10.1103/PhysRevB.55.1757

Revil, A., & Glover, P. W. J. (1998). Nature of surface electrical conductivity in natural sands, sandstones, and clays. *Geophysical Research Letters*, *25*(5), 691–694. https://doi.org/10.1029/98GL00296

Roger, G. M., Durand-Vidal, S., Bernard, O., & Turq, P. (2009). Electrical conductivity of mixed electrolytes: Modeling within the mean spherical approximation. *Journal of Physical Chemistry B*, *113*(25), 8670–8674. https://doi.org/10.1021/jp901916r

Rohatgi, A. (2015). WebPlotDigitizer (version 4) [Software]. https://apps.automeris.io/wpd4/

Romera, J. J. G. (2021). jjgomera/iapws [Software]. https://doi.org/10.5281/zenodo.4744318

Scott, S. W., Lévy, L., Covell, C., Franzson, H., Gibert, B., Valfells, Á., et al. (2023). Valgarður: A database of the petrophysical, mineralogical, and chemical properties of Icelandic rocks. *Earth System Science Data*, *15*(3), 1165–1195. https://doi.org/10.5194/essd-15-1165-2023

Sen, P. N., & Goode, P. A. (1992). Influence of temperature on electrical conductivity on shaly sands [Dataset]. *Geophysics*, *57*(1), 89–96. https://doi.org/10.1190/1.1443191

Shirozu, H. (1988). *Introduction to clay mineralogy: Fundamentals for clay science*. Asakura Publishing Co., Ltd.

Sonnefeld, J., Löbbus, M., & Vogelsberger, W. (2001). Determination of electric double layer parameters for spherical silica particles under application of the triple layer model using surface charge density data and results of electrokinetic sonic amplitude measurements [Dataset]. *Colloids and Surfaces A: Physicochemical and Engineering Aspects*, *195*(1–3), 215–225. https://doi.org/10.1016/S0927-7757(01)00845-7

Svensson, P. D., & Hansen, S. (2013). Combined salt and temperature impact on montmorillonite hydration. *Clays and Clay Minerals*, *61*(3–4), 328–341. https://doi.org/10.1346/CCMN.2013.0610412

Szczerba, M., Kalinichev, A. G., & Kowalik, M. (2020). Intrinsic hydrophobicity of smectite basal surfaces quantitatively probed by molecular dynamics simulations. *Applied Clay Science*, *188*, 105497. https://doi.org/10.1016/j.clay.2020.105497

Takakura, S. (2009). Influence of pore-water salinity and temperature on resistivity of clay-bearing rocks. *Butsuri-Tansa*, *62*(4), 385–396. https://doi.org/10.3124/segj.62.385

Tinnacher, R. M., Holmboe, M., Tournassat, C., Bourg, I. C., & Davis, J. A. (2016). Ion adsorption and diffusion in smectite: Molecular, pore, and continuum scale views. *Geochimica et Cosmochimica Acta*, *177*, 130–149. https://doi.org/10.1016/j.gca.2015.12.010

Tournassat, C., Chapron, Y., Leroy, P., Bizi, M., & Boulahya, F. (2009). Comparison of molecular dynamics simulations with triple layer and modified Gouy-Chapman models in a 0.1 M NaCl-montmorillonite system [Dataset]. *Journal of Colloid and Interface Science*, *339*(2), 533–541. https://doi.org/10.1016/j.jcis.2009.06.051

Virtanen, P., Gommers, R., Oliphant, T. E., Haberland, M., Reddy, T., Cournapeau, D., et al. (2020). SciPy 1.0: Fundamental algorithms for scientific computing in Python [Software]. *Nature Methods*, *17*(3), 261–272. https://doi.org/10.1038/s41592-019-0686-2

Voigt, W. (2020). Temperature extension of NaCl Pitzer coefficients and ΔRG°(NaCl). *THEREDA Journal*, *1–9*.

Vrolijk, P. (1990). On the mechanical role of smectite in subduction zones. *Geology*, *18*(8), 703–707. https://doi.org/10.1130/0091-7613(1990)018<0703:OTMROS>2.3.CO;2

Wackernagel, H. (1995). Ordinary kriging. In *Multivariate Geostatistics*. Springer. https://doi.org/10.1007/978-3-662-03098-1_11

Walker, E., & Glover, P. W. J. (2018). Measurements of the relationship between microstructure, pH, and the streaming and zeta potentials of sandstones. *Transport in Porous Media*, *121*(1), 183–206. https://doi.org/10.1007/s11242-017-0954-5

Watanabe, N., Yamaya, Y., Kitamura, K., & Mogi, T. (2021). Viscosity-dependent empirical formula for electrical conductivity of H2O-NaCl fluids at elevated temperatures and high salinity. *Fluid Phase Equilibria*, *549*, 113187. https://doi.org/10.1016/j.fluid.2021.113187

Watanabe, T. (2005). Electrical properties of rocks: A review. *Journal of Geography*, *114*(6), 837–861. https://doi.org/10.5026/jgeography.114.6_837

Watillon, A., & de Backer, R. D. (1970). Potentiel d'écoulement, courant d'écoulement et conductance de surface à l'interface eau-verre [Dataset]. *Journal of Electroanalytical Chemistry*, *25*(2), 181–196. https://doi.org/10.1016/S0022-0728%2870%2980336-9

Waxman, M. H., & Smits, L. J. M. (1968). Electrical conductivities in oil-bearing shaly sands [Dataset]. *Society of Petroleum Engineers Journal*, *8*(2), 107–122. https://doi.org/10.2118/1863-A

Waxman, M. H., & Thomas, E. C. (1974). Electrical conductivities in shaly sands .1. Relation between hydrocarbon saturation and resistivity index .2. Temperature-coefficient of electrical-conductivity [Dataset]. *Journal of Petroleum Technology*, *26*(FEB), 213–225. https://doi.org/10.2118/4094-PA

Wyllie, M. R. J., & Southwick, P. F. (1954). *An experimental investigation of the SP and resistivity phenomena in dirty sands* (Vol. 201, pp. 43–56). Transactions of the American Institute of Mining and Metallurgical Engineers.

Yamamoto, K., & Namikawa, H. (1994). The irreversible and reversible changes in silica glasses observed by electrical properties (Part 1), in synthetic silica glass by flame fusion [Dataset]. *Journal of the Ceramic Society of Japan*, *102*(1187), 658–664. https://doi.org/10.2109/jcersj.102.658

Zhang, H., Hassanali, A. A., Shin, Y. K., Knight, C., & Singer, S. J. (2011). The water-amorphous silica interface: Analysis of the Stern layer and surface conduction [Dataset]. *Journal of Chemical Physics*, *134*(2). https://doi.org/10.1063/1.3510536

Zhang, L., Lu, X., Liu, X., Zhou, J., & Zhou, H. (2014). Hydration and mobility of interlayer ions of (Nax, Cay)-montmorillonite: A molecular dynamics study [Dataset]. *The Journal of Physical Chemistry*, *C*, 29811–29821. https://doi.org/10.1021/jp508427c

Zheng, X., Underwood, T. R., & Bourg, I. C. (2023). Molecular dynamics simulation of thermal, hydraulic, and mechanical properties of bentonite clay at 298 to 373 K. *Applied Clay Science*, *240*, 106964. https://doi.org/10.1016/j.clay.2023.106964

Zhou, X., Liu, D., Bu, H., Deng, L., Liu, H., Yuan, P., et al. (2018). XRD-based quantitative analysis of clay minerals using reference intensity ratios, mineral intensity factors, Rietveld, and full pattern summation methods: A critical review. *Solid Earth Sciences*, *3*(1), 16–29. https://doi.org/10.1016/j.sesci.2017.12.002